UNIVERSITÉ DE MONTRÉAL

COMPARISON OF EPICARDIAL MAPPING AND NONCONTACT
ENDOCARDIAL MAPPING IN DOG EXPERIMENTS AND COMPUTER
SIMULATIONS

SEPIDEH SABOURI

INSTITUT DE GÉNIE BIOMÉDICAL

Département de physiologie

1

Abstract

Atrial fibrillation is the most common clinical arrhythmia currently affecting 2.3 million patients in North America. To study its mechanisms and potential therapies, animal models of atrial fibrillation have been developed. Epicardial high-density electrical mapping is a well-established experimental instrument to monitor *in vivo* the activity of the atria in response to pacing, remodeling, arrhythmias and modulation of the autonomic nervous system. In regions that are not accessible by epicardial mapping, noncontact endocardial mapping performed through a balloon catheter may provide a more comprehensive description of atrial activity.

In this study, a dog experiment was designed and analyzed in which electroanatomical reconstruction, epicardial mapping (103 electrodes), noncontact endocardial mapping (2048 virtual electrodes computed from a 64-channel balloon catheter), and direct-contact endocardial catheter recordings were simultaneously performed. The recording system was also simulated in a computer model of the canine right atrium.

For simulations and experiments (after atrio-ventricular node suppression), activation maps were computed during sinus rhythm. Repolarization was assessed by measuring the area under the atrial T wave (ATa), a marker of repolarization gradients. Results showed an epicardial-endocardial correlation coefficient of 0.8 (experiment) and 0.96 (simulation) between activation times, and a correlation coefficient of 0.57 (experiment) and 0.92 (simulation) between ATa values.

Noncontact mapping appears to be a valuable experimental device to retrieve information outside the regions covered by epicardial recording plaques.

Keywords: Cantact epicardial mapping, Noncontact endocardial mapping, Atrial fibrillation, Balloon catheter, Cardiac computer model

Résumé

La fibrillation auriculaire, l'arythmie la plus fréquente en clinique, affecte 2.3 millions de patients en Amérique du Nord. Pour en étudier les mécanismes et les thérapies potentielles, des modèles animaux de fibrillation auriculaire ont été développés. La cartographie électrique épicardique à haute densité est une technique expérimentale bien établie pour suivre in vivo l'activité des oreillettes en réponse à une stimulation électrique, à du remodelage, à des arythmies ou à une modulation du système nerveux autonome. Dans les régions qui ne sont pas accessibles par cartographie épicardique, la cartographie endocardique sans contact réalisée à l'aide d'un cathéter en forme de ballon pourrait apporter une description plus complète de l'activité auriculaire.

Dans cette étude, une expérience chez le chien a été conçue et analysée. Une reconstruction électro-anatomique, une cartographie épicardique (103 électrodes), une cartographie endocardique sans contact (2048 électrodes virtuelles calculées à partir un cathéter en forme de ballon avec 64 canaux) et des enregistrements endocardiques avec contact direct ont été réalisés simultanément. Les systèmes d'enregistrement ont été également simulés dans un modèle mathématique d'une oreillette droite de chien.

Dans les simulations et les expériences (après la suppression du nœud atrio-ventriculaire), des cartes d'activation ont été calculées pendant le rythme sinusal. La repolarisation a été évaluée en mesurant l'aire sous l'onde T auriculaire (ATa) qui est un marqueur de gradient de repolarisation. Les résultats montrent un coefficient de corrélation épicardique-endocardique de 0.8 (expérience) and 0.96 (simulation) entre les cartes d'activation, et un coefficient de corrélation de 0.57 (expérience) et 0.92 (simulation) entre les valeurs de ATa.

La cartographie endocardique sans contact apparait comme un instrument expérimental utile pour extraire de l'information en dehors des régions couvertes par les plaques d'enregistrement épicardique.

Mots clés: Cantact cartographie épicardique, Noncontact cartographie endocavitaire, La fibrillation auriculaire, Cathéter à ballonnet, Modèle informatique cardiaque

Table of contents

List of figures

List of tables

List of abbreviation

ATa: Area under the atrial T wave

AV: Atrioventricular

SVC: Superior vena cava

IVC: Inferior vena cava

SA: Sinoatrial

ECG: Electrocardiogram

AF: Atrial fibrillation

APD: Action potential duration

CT: Computed tomography

MRI: Magnetic resonance imaging

EAM: Electroanatomical mapping system

RAT: right atrial tachycardia

MEA: Multi electrode array

Acknowledgment

I would like to express my sincere gratitude to my advisors Dr. Vincent Jacquemet for the continuous support of my MS study and research, for his patience, motivation, enthusiasm, and immense guidance. First and most, I would like to thank him from the bottom of my heart for all their contributions, guidance, remarkable/practical ideas, and encouragement. I could not have imagined having a better advisor and mentor for my Master study. Throughout my research period, he provided encouragement, sound advices and lots of good ideas.

Thanks Dr. Vincent Jacquemet.

I would also like to thank the members of my defence committee, Dr. Pierre A. Mathieu and Dr. Philippe Comtois for taking their valuable time to examine my thesis.

My special thanks to faculty and staff of the UdeM Institute of Biomedical Engineering who have been always helpful.

My deepest heartfelt gratitude goes out to my husband, Hamid and my mother, Pooran, and my father, Kamran. Words simply cannot express my gratitude for their love and support.

Dedication

This thesis work is dedicated to my husband, Hamid, who has been a constant source of support and encouragement during the challenges of graduate school and life. I am truly thankful for having you in my life. This work is also dedicated to my parents, Kamran and Pooran, who have always loved me unconditionally and whose good examples have taught me to work hard for the things that I aspire to achieve.

Introduction

During atrial arrhythmias, electrical activity in two upper chambers of heart (atria) is chaotic and causes fibrillating (i.e., quivering) instead of achieving coordinated contraction. Repetitive episodes of arrhythmias may cause further pathological changes[1]. The autonomic nervous system, such as vagal and mediastinal nerves, can modulate electrophysiological and dynamical properties of heart[2]. The automatic nervous system also plays a significant role as a potential trigger of atrial fibrillation, especially in early stage of diseases. Therefore, knowledge about anatomy, function and electrical/mechanical activity of the heart is required for a better understanding the sources of heart dysfunction.

Our aim is to compare two cardiac mapping systems, namely contact epicardial mapping and noncontact endocardial mapping, in dog experiments and computer simulations in terms of their ability to describe and characterize atrial depolarization and repolarization. Cardiac mapping systems provide valuable tools for diagnosis and treatment of cardiac arrhythmias. In addition, many fundamental insights about atrial fibrillation can be derived from animal models. Computer models have been developed based on bioelectrical and mathematical formulation of cardiac impulse propagation to assist in interpretation of cardiac electrical activity using forward and inverse problem.

In this chapter, we will first look at heart anatomy and electrophysiology. Secondly, an introduction about cardiac mapping systems will be presented. Furthermore, we will review computer models of the heart and their applications to the interpretation of bioelectric signals. Finally, basic mathematical definitions for computation and interpretation of cardiac electrical activity called forward and inverse problems will be discussed.

1.1 Cardiac mechanical activity

Heart is a muscular organ consisting of two right and left chambers, each side consisting of an atrium and a ventricle shown in figure 1.1. Atria and the ventricles are connected through atrioventricular (AV) valves, which allow blood to circulate within the heart.
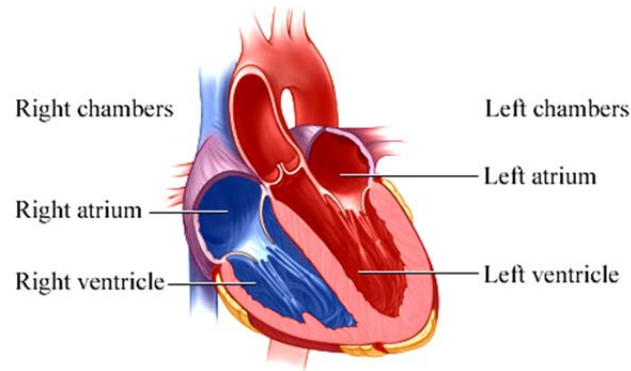
Figure 1.1- Heart anatomy include right and left atria and ventricles (Reproduced from www.webmd.com/heart/chambers-of-the-heart[3]).

Inner and outer layers of the heart are composed of cardiac muscle cells called endocardium and myocardium, respectively. The cardiac-muscle cells of the myocardium are settled in layers and make contact with adjacent cardiac-muscle cells through gap junctions, and they completely cover the cardiac chambers[4].

The function of heart is to pump oxygen-rich blood to the other organs in the body. In order to pump blood, the heart needs to complete a cardiac cycle (heartbeat) which consists of cardiac muscle contraction and relaxation. The conducting system of the atria initiates a heartbeat. The human heart beats approximately 80,000 to 100,000 a day and pumps almost 2,000 gallons of blood, which means the heart of a person living 70 to 90 years, beats approximately two to three

billion times and pumps 50 to 65 million gallons of blood[4]. A heartbeat consists of systolic and

diastolic phases (figure 1.2)[5]:

Diastole: The atria start to become filled with oxygen-poor blood, while ventricles are relax and

not contracting. At the end of this stage, atria pumps blood through the AV valves (mitral or

tricuspid valve) into the ventricles.

Systole: In this stage, ventricles contract which allows the blood to be pumped to the other

organs.
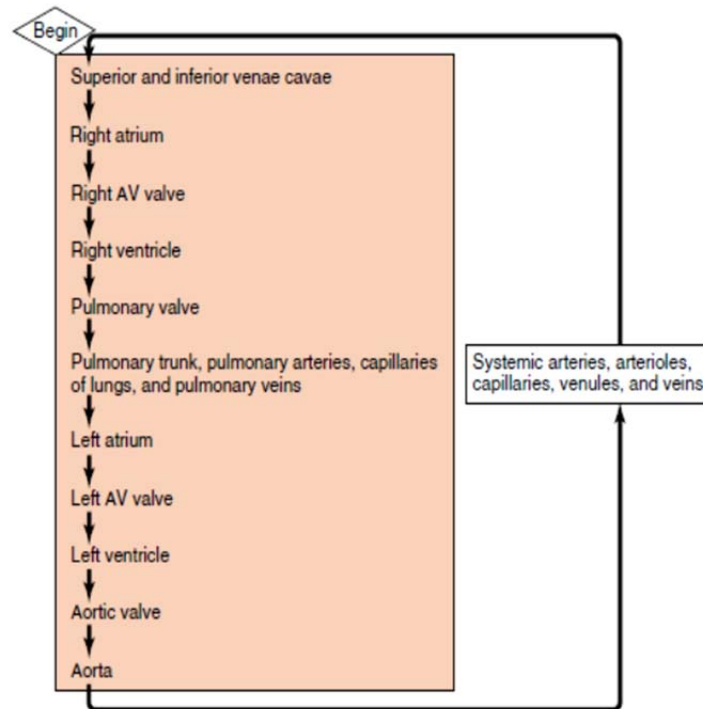
Figure 1.2- Overview of blood circulation through the heart chambers (Reproduced from Widmaier et al.[4]).

1.2 Superior and inferior vena cava

The Superior Vena Cava (SVC) and the Inferior Vena Cava (IVC) are two large veins connected

to right atrium shown in figure 1.3. These veins are responsible for bringing deoxygenated blood

to the heart. The superior vena cava carries blood from the upper part of body and the inferior vena cava carries blood from the lower part of body to right atrium.

The mapping systems we are going to use can label SVC and IVC on a reconstructed geometry representing the right atrium. These two anatomical elements will serve as reference landmarks to help identify locations within the right atrium. .

Interior View of the Heart
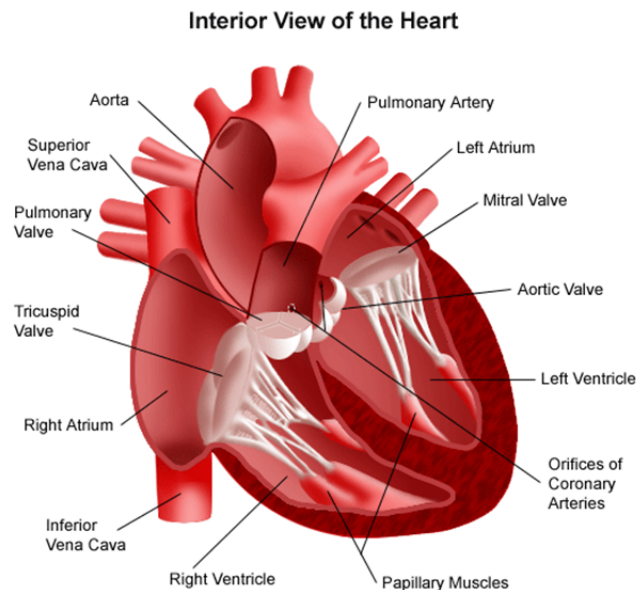
Figure 1.3- Heart anatomy; Heart veins, valves, and vessels; Superior vena cava and inferior vena cava (Reproduced from nyp.org/health/cardiac-anatomy.html[6]).

1.3   Cardiac electrical activity

As previously described, the main function of the heart, initiated by the atrial contraction followed by the ventricles, is to pump the oxygen-rich blood to body. Cardiac muscle is a smooth muscle whose contraction is triggered by the depolarization of the plasma membrane of the cardiac muscle cells. Membrane depolarization initiates a sudden increase of electrical activity, known as action potential. This initiation starts in a group of cells located in the sinoatrial (SA)

node in right atrium near the entrance of superior vena cava and propagates into and throughout the atria and then the ventricles as shown in figure 1.4[4].

The cardiac impulse travels from the SA node through the internodal pathways to the atrioventricular node (AV node). The action potential or impulse is delayed slightly at this point to allow complete emptying of atria before ventricles contract; continues through the AV bundle and down the left and right bundle branches of the Purkinje fibers. The Purkinje fibers conduct the impulse to all parts of ventricles, causing contraction.
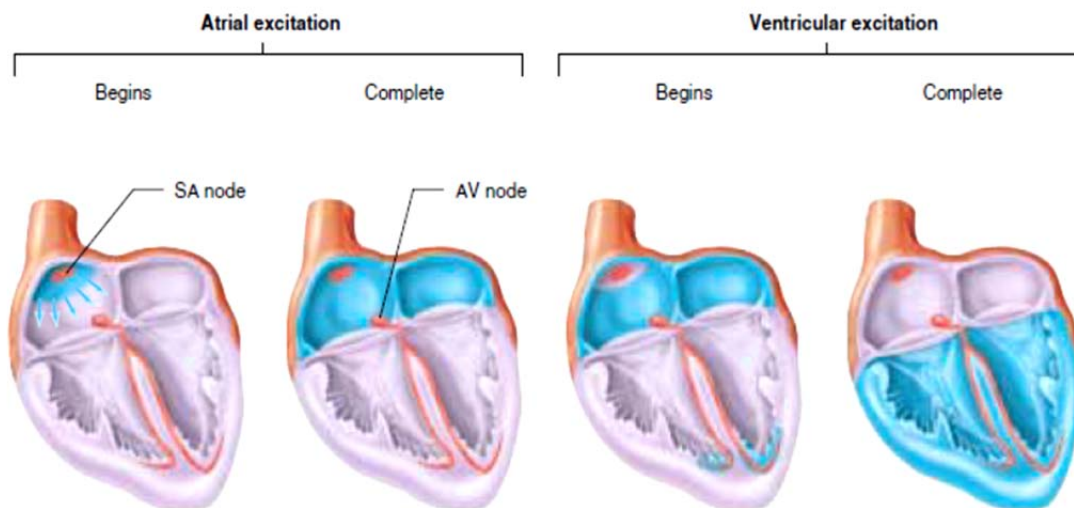
Figure 1.4- Heart electrical activity pathway; the blue color is correspond to the area that is excited by the depolarization waves (Reproduced from Widmaier et al.[4]).

1.3.1 Cardiac action potential

Typical cardiac action potentials (atrial and ventricular) are shown below in the figure 1.5.
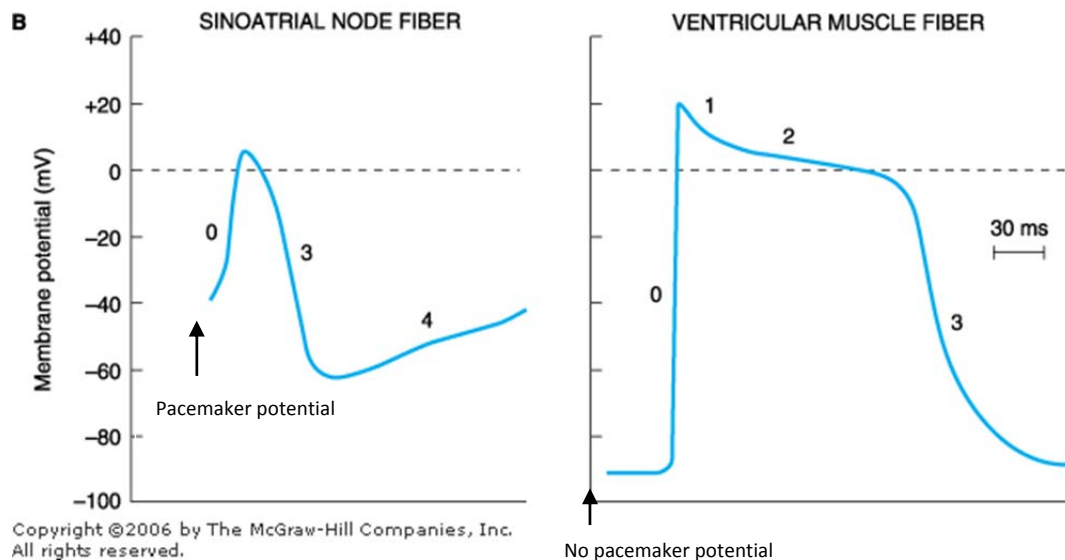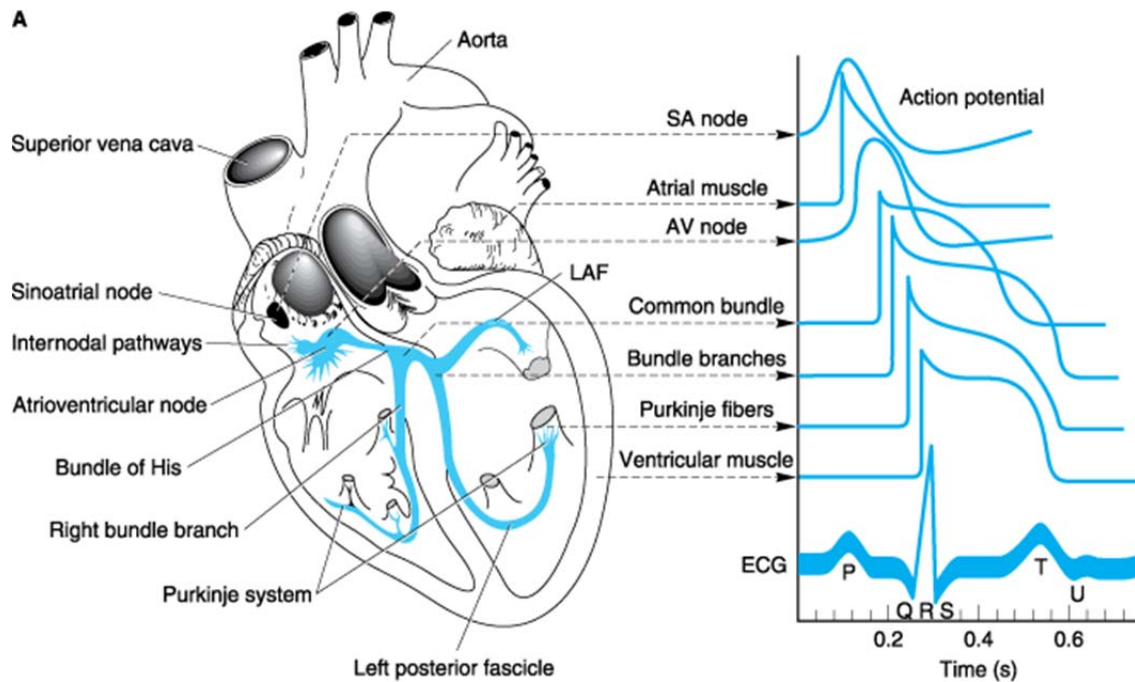
Figure 1.5- (A) Heart electrical activity path and associated action potentials have been shown by blue color. Electrocardiogram (ECG) is equal to sum of action potentials propagate in conduction path (B) Sinoatrial action potential on the left side and ventricular action potential on the right side (Reproduced from bentollenaar.com/_MM_Book/Ch.19.htm[7]).

The numbers on the action potential graphs (figure 1.5) indicate different phases:

Phase 0: Voltage-gated sodium channels open and increase the concentration of Na^+ inside the cell; at the same time, the permeability to potassium decreases. Therefore, the membrane potentials start to be positive which is termed as depolarization phase of the action potential.

Phase 1: The voltage-gated sodium channels quickly close to prevent rising sodium permeability; membrane potential decrease to 0 mV. As well, outward movement of the potassium starts in this phase by the opening of slow delayed potassium channels.

Phase 2: Calcium permeability increases which causes membrane to remain depolarized at 0 mV. As a result, the gradient of the calcium ions into the cell will be more than the gradient of the potassium ions out of the cell; known as a plateau phase.

Phase 3: The calcium channels are closed while the potassium channels are still open, consequently, the membrane permeability to calcium decreases and potential falls down to the rest potential. This process is known as a repolarisation phase.

The action potential of the cardiac cell, either atrial or ventricular cell, is similar except that the plateau phase of atrial cells is shorter than the ventricular cells. The resting potential of SA cells is not steady (upward potential drift).

Pacemaker potential is defined as threshold above which action potentials is triggered. The potential in the SA node cells spontaneously crosses the threshold to provide self-excitation or automaticity. Some cells located in the conducting system exhibit automatic activity like SA node cells; they are termed ectopic pacemakers.

The AV node - defined as an anatomical feature for electrical connection between right atrium and right ventricule - can be affected by some diseases and pharmacological substances. In our project, we disassociated the ventricular activity from atrial activity by using a drug. Consequently, the AV node could not transfer the impulse from atrial to ventricular which allowed us to isolate the atrial electrical activity.

The electrocardiogram (ECG) is obtained by the summation of the all action potentials present in the heart as shown in the figure 1.5 A. ECG is used to follow electrical events within the heart. Generally, physicians divide a normal ECG into three parts:

1) **P wave:** Atrial depolarization or atrial contraction. Usually, atrial repolarization cannot be seen in the ECG signal. It is hidden by the ventricular depolarization phase or QRS complex. It also has relatively small amplitude.

2) **QRS complex:** Usually happens after 0.15s and corresponds to ventricular depolarization or contraction. It has more deflections as compared to P wave due to the path taken by the impulse to propagate through the ventricles; lead to different depolarization waves.

3) **T wave:** Ventricular repolarization.

As already mentioned, atrial repolarization is usually masked by ventricular depolarization. Hence, we will analyze atrial electrogram waveforms outside of ventricular activity after AV node suppression to have access to atrial repolarization waves.

While the ECG can provide global information about cardiac electrical activity, it does not give detailed electrophysiological information about individual cardiac cells.

1.3.2 Heart rate

The conducting system of the heart can be affected by hormones and nerves. Neuronal elements like sympathetic and parasympathetic postganglionic fibers in the SA node can change heart rate to a much higher (over 100 beats per minute) or lower value (below 50 beats per minute) than normal condition[4]. Generally, parasympathetic activities are stronger than sympathetic activities in a healthy heart. Heart rate is increased by sympathetic nerves activation whereas; parasympathetic nerves have an opposite effect (figure 1.6).
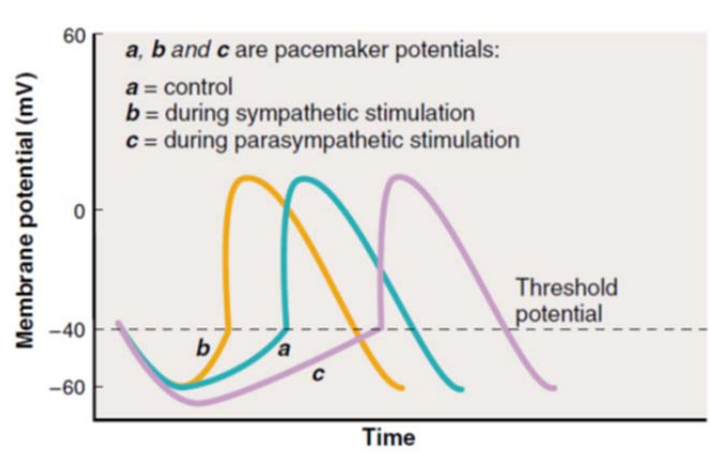
Figure 1.6- Sympathetic and parasympathetic effects on the SA node action potential (Reproduced from Widmaier et al.[4]).

As shown in the figure 1.6, the slope of the pacemaker potential increases during sympathetic nerve stimulation which cause the SA-node cells reach their threshold more rapidly. Hence, it will increase heart rate. Conversely, the slope of the pacemaker potential decreases by stimulation of parasympathetic nerves, cells reach to their threshold more slowly, and heart rate decreases.

A summary of central nervous system, branches, and their effects are described in the figure 1.7, as well as, the sympathetic/parasympathetic nerves with their connection to the heart are shown in the figure1.8.
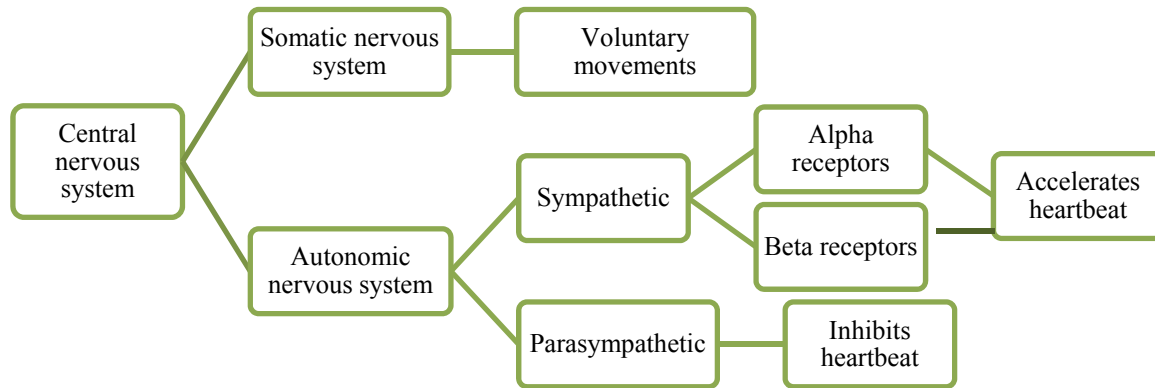
Figure 1.7- Central nervous system block diagram
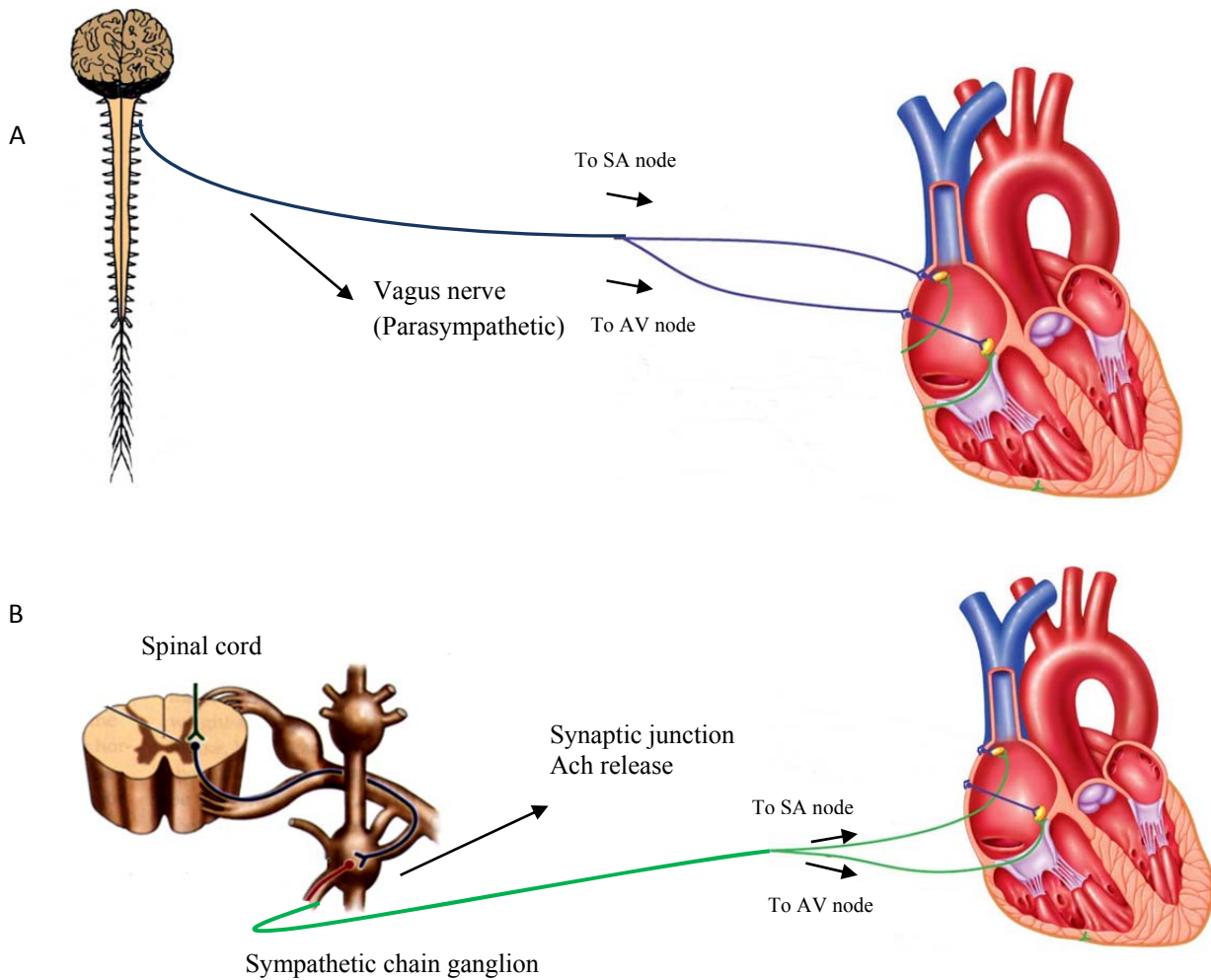
Figure 1.8- Autonomic nerves system; (A) Parasymphetic nerve (B) Sympathetic nerve from spinal cord to the heart.

The neurotransmitters released by the sympathetic and parasympathetic nerves can change the pacemaker potential. The parasympathetic neurotransmitters, like norepinephrine, increase the sodium current into the cell by opening the voltage-gated sodium channels to initiate depolarization phase. On the other hand, sympathetic neurotransmitters, such as acetylcholine, close them to prevent early depolarization phase[4].

The rate of spread of excitation (conduction velocity) through the conduction system increases by sympathetic stimulation and decreases by parasympathetic stimulation.

Table 1.2 Summary of the autonomic nerves system effects on the heart

Area affected	SA node	AV node	Atrial muscle	Ventricular muscle
Sympathetic	Increased heart rate	Increased conduction rate	Increased conduction rate	Increased Contractility
Parasympathetic	Decreased heart a	Decreased conduction rate	Decreased contractility	Decreased Contractility

1.4 Arrhythmia

An arrhythmia is a well-known heart disease, observed as an irregularity in heart rhythm including beating too fast or too slow. Several physiological and anatomical factors, such as problems with the electrical conduction system of the heart, some substances or drugs, and abnormal heartbeats may trigger cardiac arrhythmias. Mechanisms of cardiac arrhythmias include:

1) Generation of abnormal or extra excitation waves

2) Slow conduction or conduction block

3) Traveling along abnormal pathways or circuits through the heart, called reentry.

In addition, electrophysiological and neurological substrate of the heart - such as alteration of the cellular membrane kinetics, anatomical abnormalities, and perturbations of the neurovegetative balance - can initiate heart arrhythmias[8].

It has also been recognized since 1914 that atrial arrhythmias can be induced by stimulation of autonomic nervous system[9-13].

Reentry is one of the important mechanisms which can maintain important arrhythmias like atrial fibrillation, atrial flutter, atrioventricular (AV) nodal reentry, etc.[14]. In atrial fibrillation and flutter, reentrant circuits are located in the atrial myocardium. Circuits can also be found in the SA node or in the AV node (SA or AV node reentry). Finally, ventricular tachycardia is maintained by a circuit located in the ventricles.

1.4.1 Atrial fibrillation

Atrial fibrillation (AF) is the most common cardiac arrhythmia that causes 15% to 20% of strokes. AF currently affects 2.3 million patients in North America alone [15]. In the age of 50-60 and 80 years or older the prevalence are, respectively, 0.5% and 8.8%. Age, gender, race and cardiovascular diseases (hypertension, congestive heart failure, myocardial infarction, and valvular disease) are some factors that affect AF prevalence. The risk of AF development in men is higher than women at all ages[16].

AF increases risk of stroke, impairs quality of life, decreases work efficiency, and increases rates of hospitalization. In 2004, AF caused losing over 9 million working days. In 2006, estimated cost of AF-associated stroke was $12 billion[16]. AF presents a considerable challenge for patients, clinicians, and hospital managers, due to increasing prevalence, frequent complications, and large expenses. New diagnostic methods and treatments are essential to provide best care for these patients.

During AF, electrical activity in the two upper chambers (atria) of the heart is chaotic and causes fibrillating (i.e., quivering), instead of achieving coordinated contraction. Ventricular response causes poor blood flow to the body. AF may cause pathological changes (AF-induced remodeling) which include dilatation of the atrial chambers, fibrosis and loss of cell-to-cell

coupling, that can facilitate progression of the heart arrhythmias ("AF begets AF")[1]. The autonomic nervous system also plays a significant role in AF, especially at its early stage (vagal AF)[16].

The mechanisms of human atrial fibrillation are poorly understood. Moe and Abildskov[17] have defined the random propagation of multiple wavelets across the atria as AF. This hypothesis has been verified experimentally by Allessie et al[18]. They demonstrated that sustained AF consists of four or six wavelets in dogs. Clinically, different forms of AF are observed. It often starts as transient self-terminating arrhythmia and becomes more persistent with time. It may be highly symptomatic (palpitations, dizziness, fainting, fatigue, shortness of breath, chest pain), or remain completely unnoticed. It is secondary to hypertension, coronary heart disease, valvular dysfunction, or heart failure but may also occur in the absence of organic heart disease (lone AF)[16].

The presence of AF can be confirmed either in the electrocardiogram (ECG) by the absence of P waves or by an irregular ventricular rate. Therefore, biophysics underlying the P wave which is atrial depolarization and repolarization must be studied. Certainly, it helps us to discover more about the initiation of heart arrhythmias.

Action potential duration (APD)[19]can act as middle for AF development. It is defined as the time when cell reaches to the excitation threshold and starts to be depolarized till the time cell excitability is restored. APD shortening can increase the arrhythmogenicity of the substrate. Focal activation or circuits of macroreentry also promote or facilitate the initiation and maintenance of AF. Wavelength, which is defined as the distance travelled by an impulse during the refractory period, is one of the factors that affect the maintenance of arrhythmias. It is

calculated as the product of conduction velocity by refractory period. Researchers have shown that refractoriness is shorter in the left atrium than in the right atrium[20,21].The Na+ current (I_{Na}) is a significant factor leading to the conduction velocity variation. Diminishing I_{Na} can cause reduction of conduction velocity and wavelength shortens; hence, diminishing I_{Na} may help maintain AF.

The American College of Cardiology, American Heart Association, and European Society of Cardiology divide AF into three categories: paroxysmal, persistent, and permanent[22]. A recurrent wavelet self terminates in less than 7 days is paroxysmal AF. Localized sources leading to fibrillatory conduction cause paroxysmal AF. Moreover, random multiple-wavelet reentry decreases the likelihood of self-termination. A recurrent wavelet for more than 7 days is called persistent AF. Permanent AF means that the recurrent wavelet is present in the long term and the heartbeat cannot be reverted back to a normal rhythm.

Understanding the electrophysiology underlying heart action potential like depolarization and repolarization phases, APD, conduction velocity etc. not only can help physicians for detection of ectopic beat and making a good surgical ablation strategies but also engineers can have better understanding of AF mechanisms, and consequently, they can design better future catheters used in treatments.

1.5 Heart mapping system

Heart mapping systems allows physicians and scientists to investigate heart diseases, notably heart rhythm disturbances. In this section we will look at the heart anatomical and electrophysiological mapping technologies and their role in understanding the genesis of arrhythmias.

1.5.1 Cardiac anatomical imaging system

1.5.1.1 Fluoroscopy

Fluoroscopy uses x-ray to visualize the motion of liquid and anatomical structure of a patient. This system has been the first imaging system used in catheter ablation procedure of atrial fibrillation. Catheter ablation procedure using fluoroscopy is shown in the figure 1.9. The radiation exposure time is critical for patient and operator safety during ablation, especially for long and repetitive procedures.
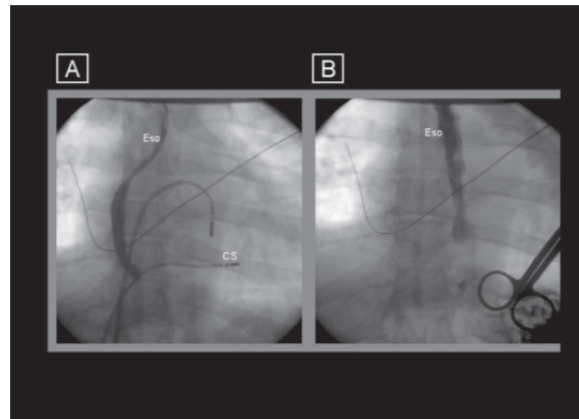
Figure 1.9- Ablation procedure is shown by fluoroscopy imaging system. **A:** Before ablation. **B:** After ablation. CS: coronary sinus catheter. Eso: esophagus (Reproduced from Natale et al.[22]).

1.5.1.2 Computed tomography

Cardiac computed tomography (CT) system is a non-invasive heart imaging system that uses an x-ray machine rotates around patient body and takes clear and detailed picture of the desired organ. CT can be used to reconstruct the geometry of pulmonary veins since it is the major anatomical region in the atria with high likelihood of atrial fibrillation triggers (figure 1.10). These images can be used for AF treatment notably navigation of the catheter during ablation procedure. However, access to the anatomical structure alone is not sufficient to identify cardiac diseases.
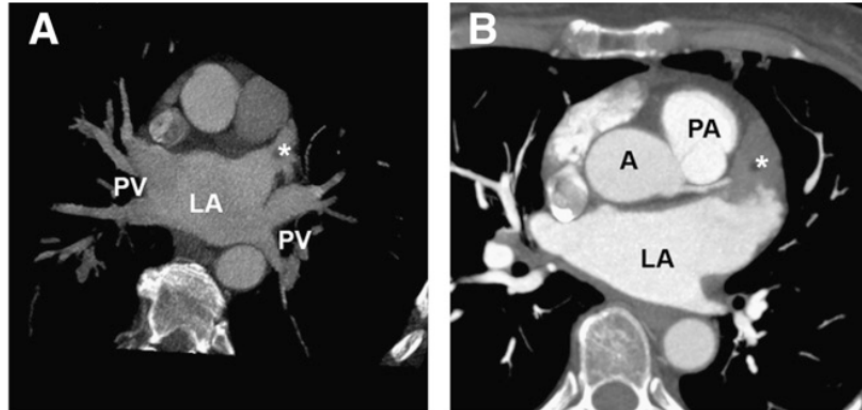
Figure 1.10- (A) 4 healthy Pulmonary veins captured by CT. (B) Pulmonary vein of a patient with AF before undergoing radiofrequency ablation. Asterisks show the left atrial appendage A: healthy B:throumbus(Reproduced from Prat-Gonzalez et al[23])

1.5.1.3 Magnetic resonance imaging

Magnetic resonance imaging is a non-invasive and radiation-free system for generating organ and tissue images. Cardiac MRI has been used to obtain pictures of the beating heart and to evaluate its structure and function. Mostly, MRI is used to improve treatment procedure such as radiofrequency ablation by its role in pre-surgical planning, preacquired anatomical mapping used during the procedure itself, and post-surgical confirmation of the integrity of the procedure. MRI images with 3-D electroanatomical navigation systems such as CARTO XP EP Navigation System by Biosense Webster and EnSite™ System by St. Jude Medical can be an excellent combination to facilitate catheter navigation, pre-procedure planning, and therapy delivery for arrhythmia (figure 1.11).

3D bipolar voltage map   3D MRI LV reconstruction   MRI native view
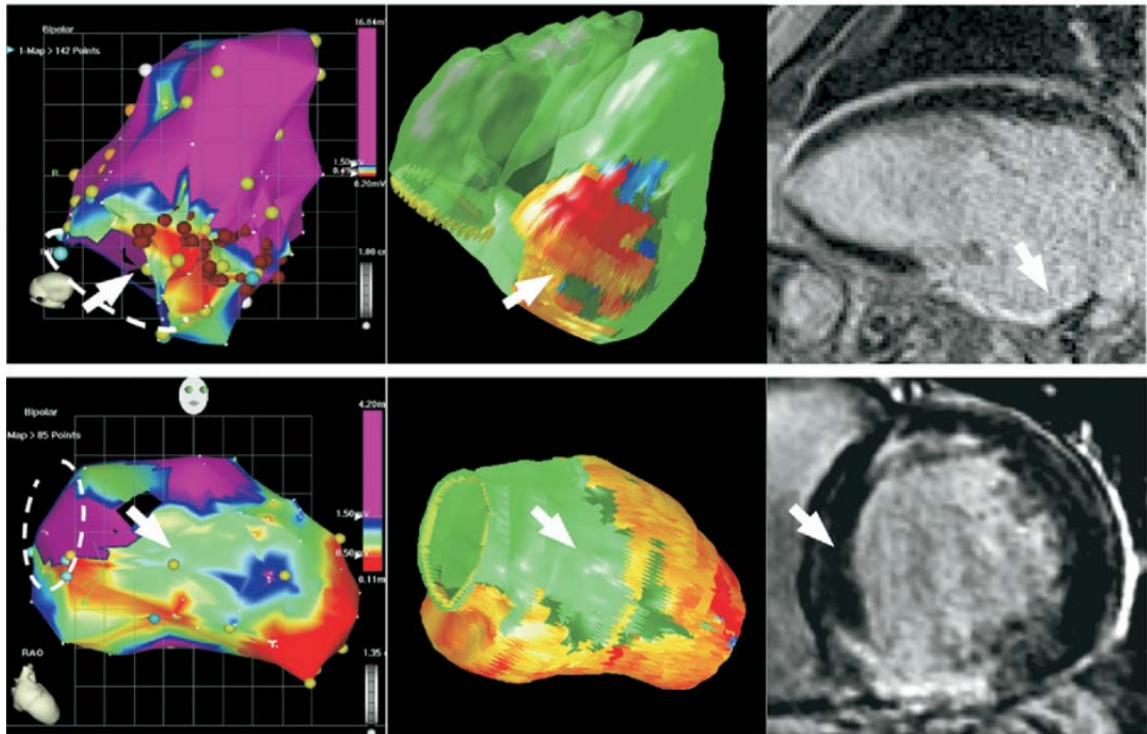
Figure 1.11- Left panel is CARTO bipolar map and right panel is MRI images. The arrows indicate the location of scar in the two systems which is miss matched (Reproduced from Cordreanu et al.[24]).

1.5.2 Three dimensional electroanatomical mapping system (EAM)

Why AF is difficult to treat? one of the reasons is that we lack a good understanding of its causes. AF can change the pathophysiological and electrophysiological aspects of underlying tissue (remodeling) which results in other electrical and mechanical adaptations that aggravate the vulnerability to AF. One option to determine and observe degree of remodeling is to measure electrical changes from the inside of the heart by means of electroanatomical mapping systems.

Electroanatomic mapping systems (EAM) include Biosense CARTO, EnSite/NavX, Non-contact mapping, and Real-Time position management system. They are used to gain access to the electrophysiological substrate of the heart. They display activation and propagation maps on three dimensional geometry of cardiac chamber of interest by non-fluoroscopic catheter. This

facilitates and increases accuracy of ablation procedure. Each EAM system has its own strengths and weaknesses, and should be chosen based on the information that we need (activation mapping, substrate mapping, and cardiac geometry) for therapy.

The EAM systems allow operators to observe the location of origin of arrhythmia or ectopic beat in cardiac chamber geometry and catheter manipulation without fluoroscopic guidance. EAM system advantages such as less fluoroscopy time, less radiation dose, and procedure time have been proved by several studies. The most significant of these is its application to treatment of atrial fibrillation[25-33].

In summary, here are the main advantages of EAM as compared to the conventional mapping system:

1. Facilitates cardiac arrhythmia mapping and ablation procedure

2. Reduced fluoroscopy time

3. Radiation dose

4. Procedure time

In our study, we used EnSite NavX system to preform catheter navigation and localization in the canine right atrium. It was also used to reconstruct canine right atrium geometry for creating the computer model which will be discussed in the method section.

1.5.2.1 Contact epicardial mapping

Epicardial mapping is an experimental tool to study the electrophysiological characteristics of the atrial fibrillation. This system simultaneously records electrical activity from several or even hundreds of electrodes placed directly on the epicardium during open-chest surgery. We need information from all anatomical location of the heart for mapping characteristics of AF- chaotic

and rapidly changing of activation. Our system (Figure 1.12) consists of 5 silicone plaques with 191 unipolar recording contacts (4.6–5.9 mm spacing) were positioned on (1) Bachmann bundle and adjacent base of the medial atrial appendage on the right and the left side, (2) the right atrial free wall and lateral right atrial appendage, (3) the left atrial free wall, (4) the lateral left atrial appendage, (5) the dorsal left atrial wall between the pulmonary veins to cover entire atria.

Contact endocardial mapping is also possible using an inflatable balloon constructed with nylon and with 64 electrodes placed on its surface[34]. This balloon is inserted in the atrial chamber through an incision in the atrial appendage. The balloon is inflated to ensure contact with the endocardium. Continuous recording over multiple beats is difficult since the balloon has to be deflated to avoid affecting too much cardiac hemodynamics.

(A)   (B)
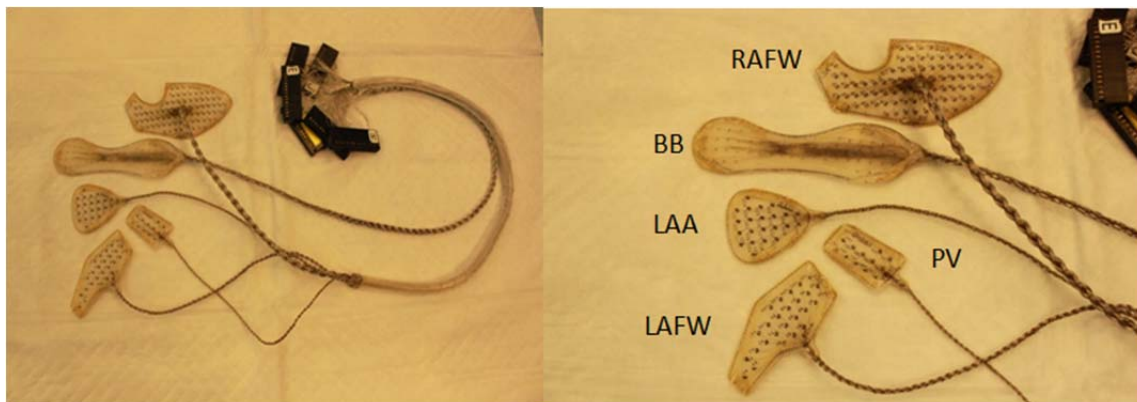
Figure 1.12- (A) Epicardial mapping system; (B) Five epicardial electrode plaques include: LAA, RAA—left and right atrial appendage; LAFW, RAFW—left and right atrial free wall; BB—Bachmann bundle; PV—pulmonary veins

1.5.2.2 Non-contact endocardial mapping

The EnSite Array multielectrode array (MEA; Endocardial Solutions, St. Jude Medical, Inc., St. Paul, MN, USA) is a new technology for non-contact cardiac electroanatomic mapping (figure 1.13). It has been Introduced in 2001[35] and is able to produce three dimensional pictures of the electrical activity of the cardiac chamber of interest.

Figure 1.13- Non-contact mapping system; Balloon catheter; Asterisks are two rings electrodes that are used to construct cardiac geometry.

Non-contact mapping system includes a computer workstation that is used to display three dimensional maps of cardiac electrical activity, custom designed amplifier system, with a balloon shape multi-electrode array catheter (MEA) to map endocardial activation.

The MEA is a collapsible balloon-shaped catheter consisting of 64 intersecting electrodes on its surface which will be expanded once located in the cardiac chamber of interest. The electrical potential present on the MEA's surface is recorded, permitting calculation of the endocardial potential by solving an inverse problem (see section 1.7). This allows reconstruction of electrograms at endocardial sites in the absence of physical electrode contact at those locations. MEA position in the chamber is identified by applying a low level 5.6 kHz current in two ring electrodes along its shaft and measuring the resulting potential on the body surface. Finally, moving the mapping catheter along the endocardial surface helps to reconstruct chamber geometry (figure 1.16 (asterisks)).

Recording cardiac electrical activity from thousands of points simultaneously and enabling reconstructing over 2048 electrograms from a single beat are two of the most elegant abilities of the non-contact mapping system. For these reasons, non-contact mapping has been validated for its application in human ventricles and atria[36-40]. It has been also validated in a human study for reconstruction of the endocardial electrograms in human left ventricular during sinus rhythm[41].

It has been demonstrated that non-contact endocardial mapping is practical in the diagnosis and treatments (such as catheter ablation) for various cardiac arrhythmias[35] including atypical right atrial flutter[42], focal right atrial tachycardia (RAT)[43], right ventricular tachycardia[44,45], left atrial tachycardia[46] and atrial fibrillation[36,47,48]. Non-contact endocardial mapping has been used in different types of arrhythmias for the purpose of investigation and treatment. For example, the circuit of the right atrial flutter and the zones of the slow conduction have been identified using non-contact endocardial mapping system for performing radiofrequency ablation[49,50].It is also able to show the macroreentry circuit during atrial flutter even with functional and anatomical variations between different patients[51].

The majority of the researches by this new catheter were done in right atrial (56%) due to anatomical limitation of the left atrium; thus its application in the left atrial still needs more investigations[35].

From the treatment point of view, most important advantages of non-contact endocardial mapping are tracking an arrhythmia and guiding an ablation catheter by a single beat. In addition, construction of 2048 signals from one beat allows precise mapping even in a patient with rare focal activity. Fluoroscopy time, radiation dosage, and procedure time are reduced by using non-contact mapping conjunction with conventional mapping strategies[52]. Other useful features are:

radiation-free catheter navigation, re-visitation of points of interest, and cataloging ablation points on the three dimensional model.

Non-contact endocardial mapping has a good precision in recording the endocardial potential at distance <40 mm from the MEA; hence, the equator of the MEA ought to be placed close to the area of interest [47,53,54]. Earley *et al.* used non-contact endocardial mapping to map the permanent AF and validate noncontact mapping. Based on their work, the signal morphology, correlation and the timing are strongly dependent on the distance of the balloon catheter from the recorded point[38]. Hindricks *et al.* had 17 patients with episodes of paroxysmal atrial fibrillation who underwent non-contact mapping of the left atrium to identify the localization of pulmonary vein foci that initiate paroxysmal atrial fibrillation[36].

Disadvantages of this technique can be listed as: 1) inaccuracy of the recorded potentials in terms of time and morphology at great distances from the MEA, 2) limited accuracy of the reconstructed signal because it is the solution to an inverse problem which is an ill-posed problem, 3) difficulty in deployment of the balloon catheter into the atria, 4) inaccuracy in recording the electrical potentials in certain atrial geometry like appendages and 5) the possibility of inducing non-sustained arrhythmia by MEA[36].

On the other hand, the conventional mapping technologies, like CARTO, can only map one location at time. Therefore, it is time consuming and, sometimes, mechanical induction of ectopic activity might occur during localization of arrhythmogenic foci.

Atrial fibrillation is often triggered by ectopic foci in pulmonary veins for that reason, this focal triggers are typically targeted by ablation strategy[55].

Ectopic foci are critical points for designing ablation strategy. Hindricks et al. have determined the location of pulmonary vein foci by using noncontact mapping[36] and , ability of the system to identify scar and low voltage areas in right atrial has been proved[53].

1.6 Computer modeling

The electrophysiological and neurological mechanisms underlying cardiac arrhythmias are complicated. Investigations about cardiac arrhythmias can be performed in patients, in animal models, or in computer models. Testing a new approach or technology in patients is not trouble-free and cost efficient. Hence, a combination of animal models and computer models may provide more details about electrophysiological and neurological mechanisms underlying heart functionality and cardiac arrhythmias like atrial fibrillation.

Computer models of the heart allow us to selectively change the local properties of ionic channels and set it to work only on the target that we are interested in. This option reduces confounding effects related to the physiological substrate. Changing the electrical properties of individual cardiac cells can set the stage for AF. Each cardiac cell contains a large number of ion channels of different types, and the proper function of a cardiac cell depends on a choreography involving all of these ion channels i.e. the proper number of each type of ion channels, the individual channels that must open and close at the proper time. Consequently, by ionic channel manipulation, the conditions necessary for a re-entrant arrhythmia or AF may be created.

Computer simulation of function of the heart offers the potential to guide disease treatment and management, to clarify the causes creating these conditions and eventually, to develop new treatment tools and drugs to reduce their threat to life.

The heart modeling steps can be summarized in the following chart[8]:

In order to achieve a predictive model of the heart, we should first consider the electrophysiological details about cardiac cell i.e. ions fluxes across membranes and from cell to cell.

```
Molecular   →   Membrane   →   Cell level   →   Tissue level   →   Organ level
level           model
```

The first atrial cell models were developed using rabbit atrial cells by Hilgemann *et al.*[56] and Lindblad *et al.*[57] Later, Nygren *et al.*[58] and Courtemanche *et al.*[59] introduced two human atrial cell models. The Courtemanche model can be modified to produce atrial arrhythmias and incorporate the effect of acetylcholine (vagal stimulation) [58]. Moreover, a canine version of the model has been created.

Excitable cells are connected through gap junctions. The interconnections of the cellular network form the cardiac tissue. Action potential propagates from cell to cell by this pathway. When this network is approximated by a continuous conductive medium, impulse propagation is governed by the monodomain or bidomain equations (nonlinear partial differential equations of the reaction-diffusion type)[8].

The geometry of atria has been constructed using different medical imaging modalities like magnetic resonance imaging[60,61], electroanatomical mapping system, computer aided tomography[62], and dataset resulting from Visible Human project[63-66].

The computer models are able to simulate heart disease, genetically modified cells, and regional heterogeneity by changes in membrane kinetics[8], mainly ionic currents which have a significant impact on the repolarization phase of the action potentials and on the occurrence of conduction

block or reentry[67-70]. They have been used to study the effect of cardiac cell remodelling- a pathophysiological adaptation of the atrial cells to the fibrillatory rhythm[8].

As already mentioned, the autonomic nervous system has a complementary role to create AF substrate. Vagal stimulation and acetylcholine (ACh) concentration can change rhythm adaptation and spatial heterogeneity in the heart. Computer models provide a framework to investigate the role of nervous system in atrial arrhythmias. For instance, Vigmond et al. induced reentries in a 3-D canine atrial model by modulating ACh [71].

In this work, we are going to create an electro-anatomical computer model of canine right atrium based on geometrical data acquired from catheter localization system (EnSite NavX). This model will be used to generate contact and noncontact (epicardial/endocardial) signals to validate and evaluate the signal processing tools and relevance of the both mapping systems.

In the next section, we are going to define the concepts used to compute electrical signals in noncontact mapping system and produce a mathematical model of the heart.

1.7 Forward and Inverse problem

In recent years, scientists have applied mathematics for visualizing important electrical phenomena in the human heart. As mentioned earlier, the heart is a pump that works efficiency if the conduction system sends impulse properly. Electrical impulse starts from the SA node and propagates throughout the whole heart, causing contraction in heart muscle. Distribution of these waves in the heart is termed heart electrical activity which reflects to the chest, which allows physicians to measure electrical potential called an electrocardiogram or ECG.

1.7.1 Forward problem

Computing electrical potentials on the thorax surface (body surface potential) from heart surface

potentials is known as the forward problem of electrocardiography (figure 1.14). One of the main

applications of the forward problem is in the simulation of ECG signals in computer models and

studying the effects of torso inhomogenities on the ECG. The solution to the forward problem

entails surface methods and volume methods. More detail information about these methods can

be found in [72].
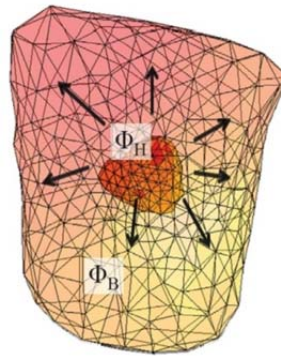
Figure 1.14- Definition of the Forward problem. Arrows indicate the direction of computation which is from heart surface potential to the body surface potential; $\emptyset_H$ is heart surface potential and $\emptyset_B$ is body surface potential (Reproduced with permission from Cluitmans et al.[73]).

However, application of forward problem in medical domain is limited since we need

information about heart surface potentials and electrophysiological activity of the heart, notably,

the potentials at the outer heart wall (the epicardium). Hence, computing heart surface potentials

from body surface potentials is desirable for clinical applications[72].

1.7.2 Inverse problem

The inverse problem consists in predicting electrical potentials on the heart surface using

electrical potential on the body surface (Figure 1.15).
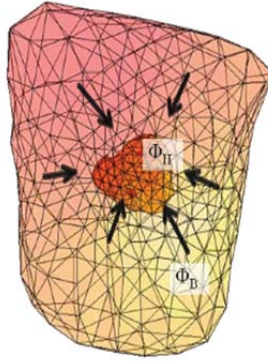
Figure 1.15- Definition of the inverse problem; Arrows indicate the direction of computation which is from body surface potential to the heart surface potential. $\emptyset_H$ is heart surface potential and $\emptyset_B$ is body surface potential (Reproduced with permission from Cluitmans et al.[73]).

The procedure of reconstructing heart surface potentials or solving the inverse problem is illustrated in the figure 1.15. [74] Briefly, it starts by acquiring potential recordings (ECGs) on the body surface of a patient, finding the anatomical relationship between the heart and body surface (transfer matrix) which requires generating a patient-specific model of the torso, and finally reconstructing the heart surface potentials (epicardial) using mathematical techniques (pseudo-inverse and regularization) (figure 1.16).

In our project, the balloon catheter was located in the cardiac chamber and the endocardial activity was computed by means of an inverse problem (figure 1.17).
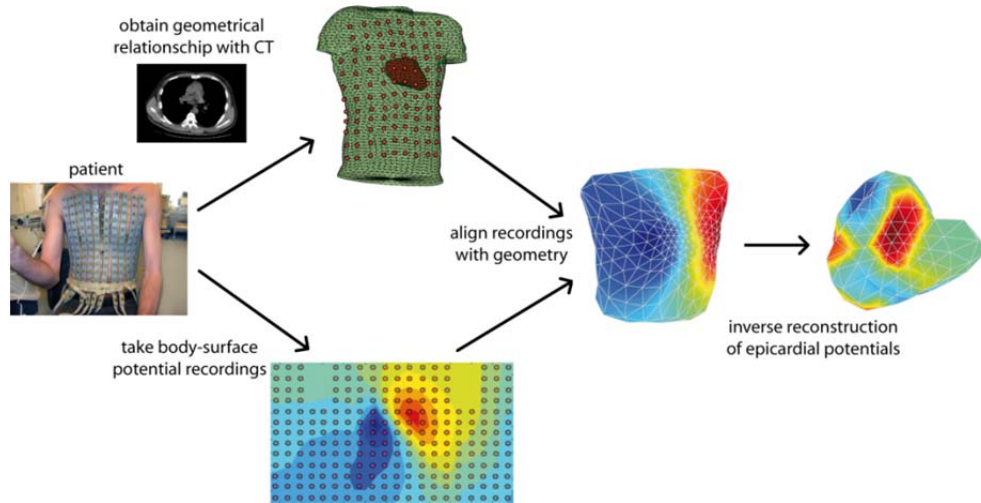
Figure1.16- Application of inverse problem in electrocardiography. The procedure of reconstruction of heart surface potential from body surface potential (Reproduced with permission from Cluitmans and et al.[73,75]).
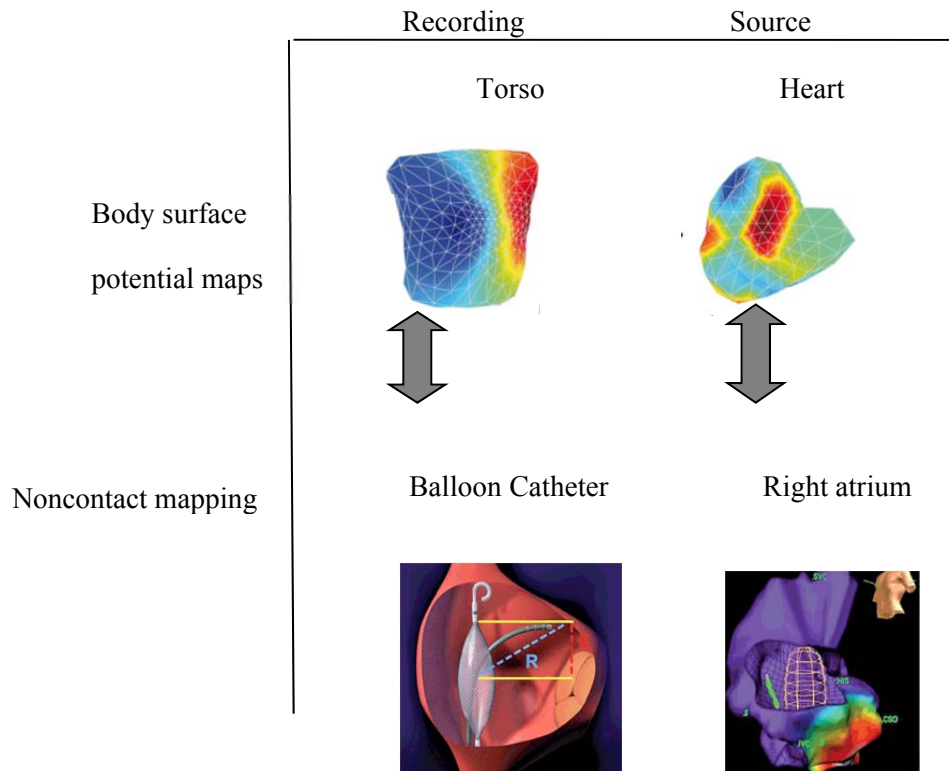
Figure 1.17- Application of inverse problem in noncontact mapping; Balloon catheter inside the cardiac chamber and compute the endocardial potential by using inverse problem (Reproduced with permission from Cluitmans and Salinet et al.[73,75]).

In figure 1.17, electrical potential is recorded from chest and balloon catheter, respectively, for body surface potential maps and noncontact mapping. Next, heart and right atrium endocardial electrical activity are reconstructed from the recorded electrical potentials -from the chest and balloon catheter- by means of inverse problem.

Nowadays, medical companies are interested in non-invasive technology and also other similar procedures due to their unique properties. Any successful demonstration of application of this technique would significantly advance cardiac diagnostic procedures. Unfortunately, up to now in most cases the quality of reconstructed electrical potentials has not been satisfactory enough for a reliable diagnosis[72].

The main source of the difficulty stems from the fact that the inverse problem in cardiac electrophysiology is well known to be a mathematically ill-posed problem; i.e. its solution can oscillate wildly with the slightest noise or measurement errors or it is not unique or even exists. The number of parameters in the desired solution, i.e. the complexity of the assumed heart model, can change the ill-posed nature of the inverse problem. Therefore, the solution to the inverse problem may vary depending on the assumptions of the computer model[72].

In order to remove ill-posed nature of inverse problem the desired solution needs to be stabilized by a mathematical technique known as regularization.

The solutions to the inverse problem may be based on [70]:

1) Multipole coefficient

2) Moving-dipole inverse solutions

3) Multiple-dipole inverse solutions

In our project, forward problem was used to compute the electrical potential appearing on the surface of the balloon catheter (64 electrodes) and the electrical potential of 103 electrodes on the 2 silicone plaques, for noncontact endocardial and epicardial mapping respectively.

Right atrium endocardial electrical activity (2048 signals) was reconstructed from electrical activity recorded by 64 electrodes on the surface of balloon catheter by solving an inverse problem.

These methods provide comprehensive information about cardiac electrophysiological activity.

1.8   Signal processing tools

In this section we are looking at basic principles underlying intracardiac electrogram analysis and their technical applications in cardiac electrophysiology. To describe atrial depolarization and repolarization, two parameters have been considered in this study: activation time and area under the atrial T waves (ATa). These parameters provide basic information about normal and abnormal electrophysiological properties.

1.8.1 Activation time

Activation time is one of the most fundamental factors to describe the mechanisms of atrial arrhythmias. For instance, identifying the earliest activation site by mapping activation time is essential for ablation procedure to recognize sites of ectopic beats. The concept of activation time is defined in figure 1.18 for a unipolar electrogram[76].

Electrode

Action potential

Activation time is the moment when
the action potential passes underneath
the electrode
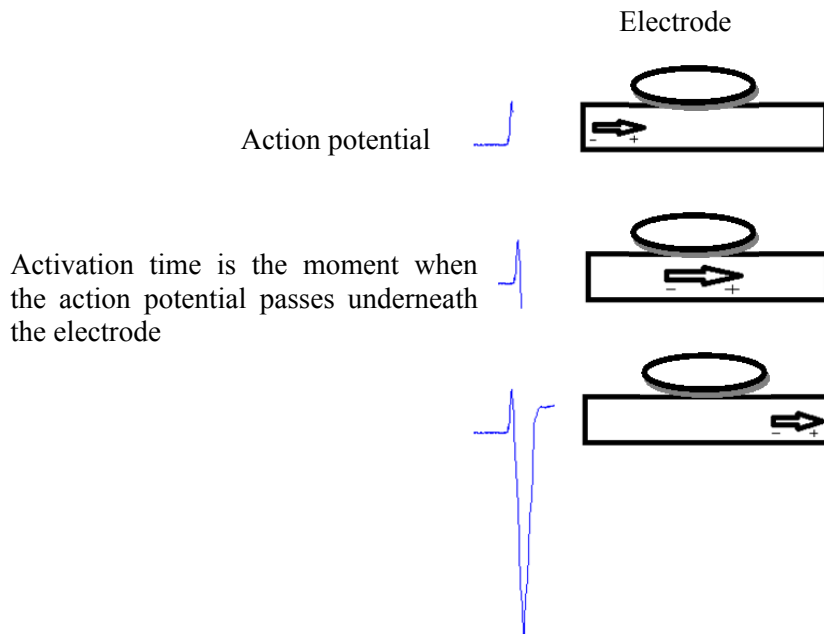
Figure 1.18- The concept of activation time. (A) Activation is going to reach to cell beneath the electrode (Depolarization phase). (B) Activation has reached beneath the electrode (Plateau and repolarization). (C) Activation is going to pass to adjacent cells (Rest).

Activation time was defined as the time where the peak negative derivative reach the maximum value and validated by Ndrepepa[77] using extracellular electrograms. It has been recognized as the most accurate indicator of activation beneath the electrode, and is supported by both experimental and theoretical work[77-80].

In figure 1.19, the first signal represents an atrial depolarization and the red point indicates the activation time. The red point is located at the peak negative in the panel B. The last signal is the transmembrane potential that indicates the cellular activation beneath the electrodes after red point or activation time (the extracellular potential is directly proportional to the second temporal derivative of the intracellular potential).

The maximum negative derivative of an electrogram corresponds to the upstroke of action potential
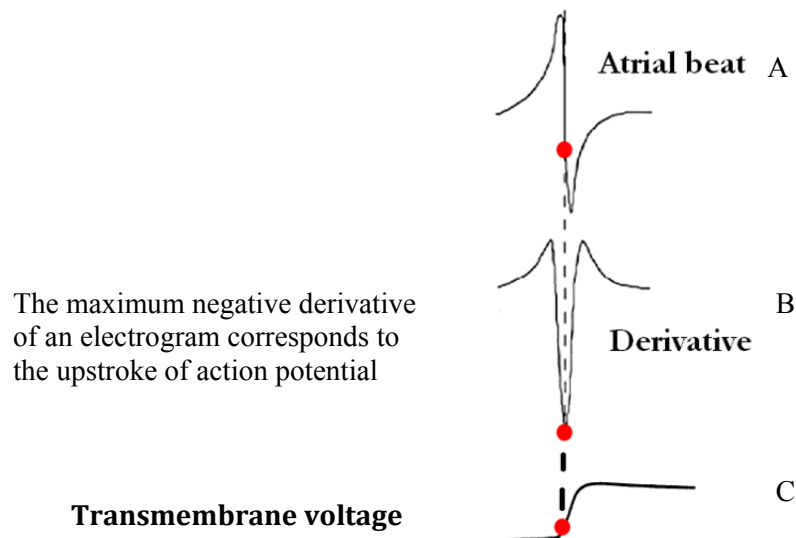
Figure 1.19- Activation time mathematical definition is shown by red dot. (A) An atrial beat. (B) Derivative of A. (C) Transmembrane voltage.

Mapping of activation sequence has been studied in epicardial and endocardial signals in the isolated canine right atrium to determine the concordance between epicardial and endocardial activation times. The difference between epicardial and endocardial activation was small during sinus rhythm but can be significant during arrhythmias[80].

Armour et al used epicardial and non-contact endocardial mapping to identify the sites of origin of sinus or ectopic beat preceding atrial fibrillation. They also have shown the contribution of the efferent neuronal elements in electrophysiological substrate of the atrial tachyarrhythmias[81].

In order to map the activation time sequence of the endocardial surface of cardiac chamber, we can use cardiac anatomical mapping systems by either one catheter or multielectrode catheter. A balloon catheter with 64 electrodes was used in our study. In addition, three dimensional color coded maps was reconstructed using electroanatomical mapping system (EnSite array).

Our aim is to compare two cardiac mapping systems in term of activation times by analyzing right atrium beats in canine experiments. To avoid having ventricular beat mask relevant atrial activity (notably repolarization), atrial activity was disassociated from ventricular activity by pharmacological suppression of the AV node and ventricular pacing. Ventricular beats remained present but were not synchronized with atrial repolarization. In order to choose appropriate beats in which ventricular beats were located far enough from atrial beats (250-300 ms later), activation times and ventricular beats were plotted for each catheter location and for all experiments as shown in figure 1.20. For instance, the time interval between activation time and ventricular beat is less than 300 ms in beat number 1, 2, 3 in the figure 1.20 (A), therefore, beat number 4and 5 were chosen for this case.
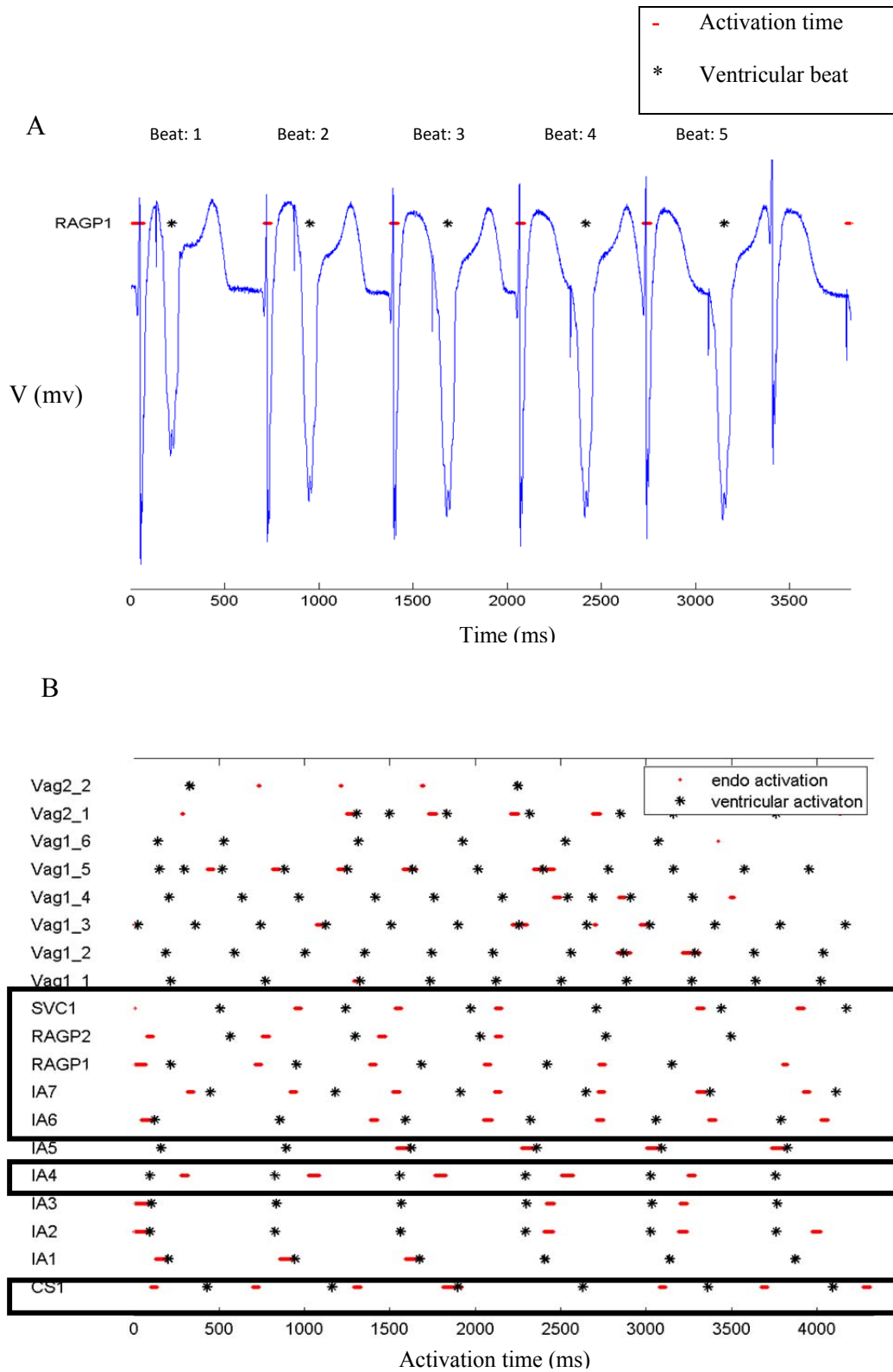
Figure 1.20- Activation times and ventricular beats are plotted for (A) Right ganglionic plexus and (B) for all experiments.

In order to choose the corresponding beats between epicardial and non-contact endocardial signals, the delay between these two mapping system was calculated then the activation times were plotted for all experiments in figure 1.21.
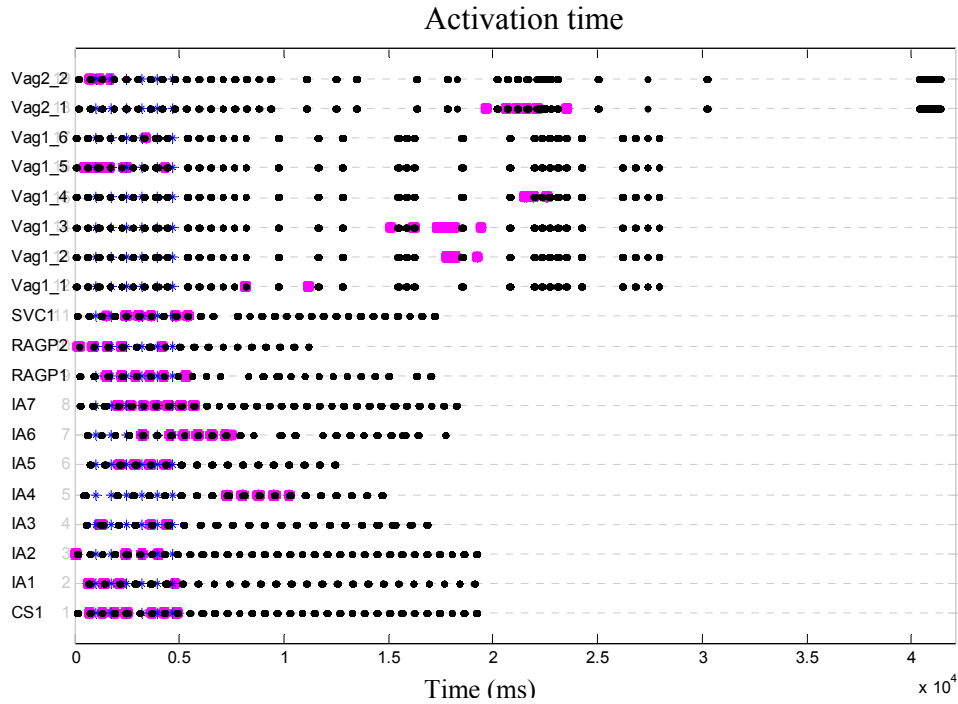
Figure 1.21- Concordance between epicardial and non-contact endocardial activation times for all catheter locations; The purple dots are non-contact endocardial activation times, the black dots are epicardial activation times, and blue stars are ventricular beats.

In addition, activation times were plotted for each catheter location separately, as seen in the figure 1.22. Also, we mapped them on the epicardial and endocardial geometry to ensure that the correspondent beats were chosen.

For example, the activation times for both mapping systems are plotted for catheter located in the right atrium ganglionated plexus in figure 1.25. Beats number 1 to 4 of the epicardial signals

correspond to beats number 1 to 4 of the endocardial signals in figure 1.25(A). Meanwhile, the earliest activation time happens near the SVC for both mapping systems (shown as asterisks).
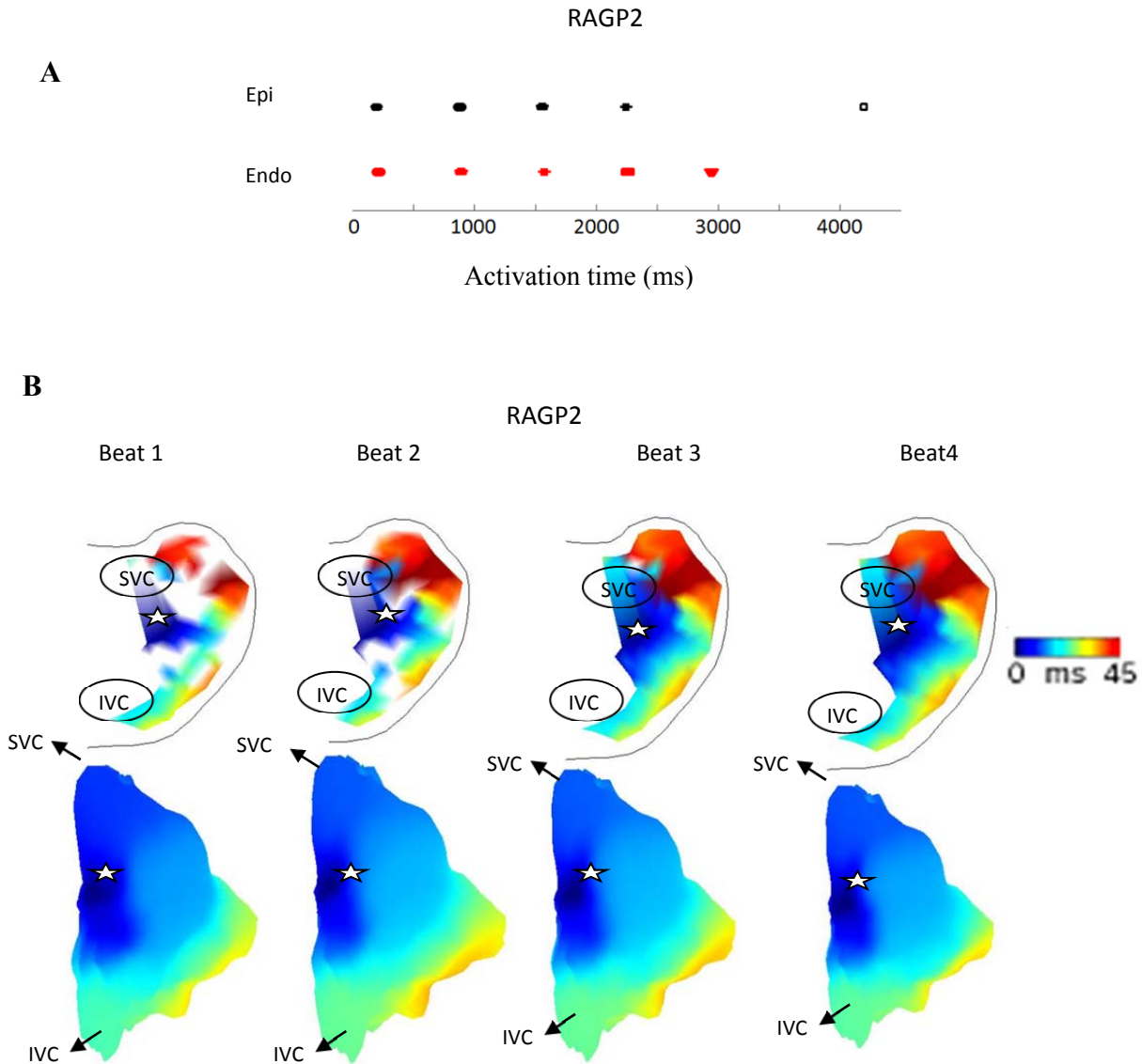
Figure 1.22- Experimental activation times; (A) Activation times are plotted for one catheter location to notice the correspondence between the beats. (B) Activation times are mapped for the same beats. Anatomical locations are shown by the stars and arrows. SVC superior vena cava; IVC inferior vena cava, RAGP right atrium ganglionated plexus (catheter location).

The same procedure was done for the simulated epicardial and endocardial signals shown in figure 1.23.
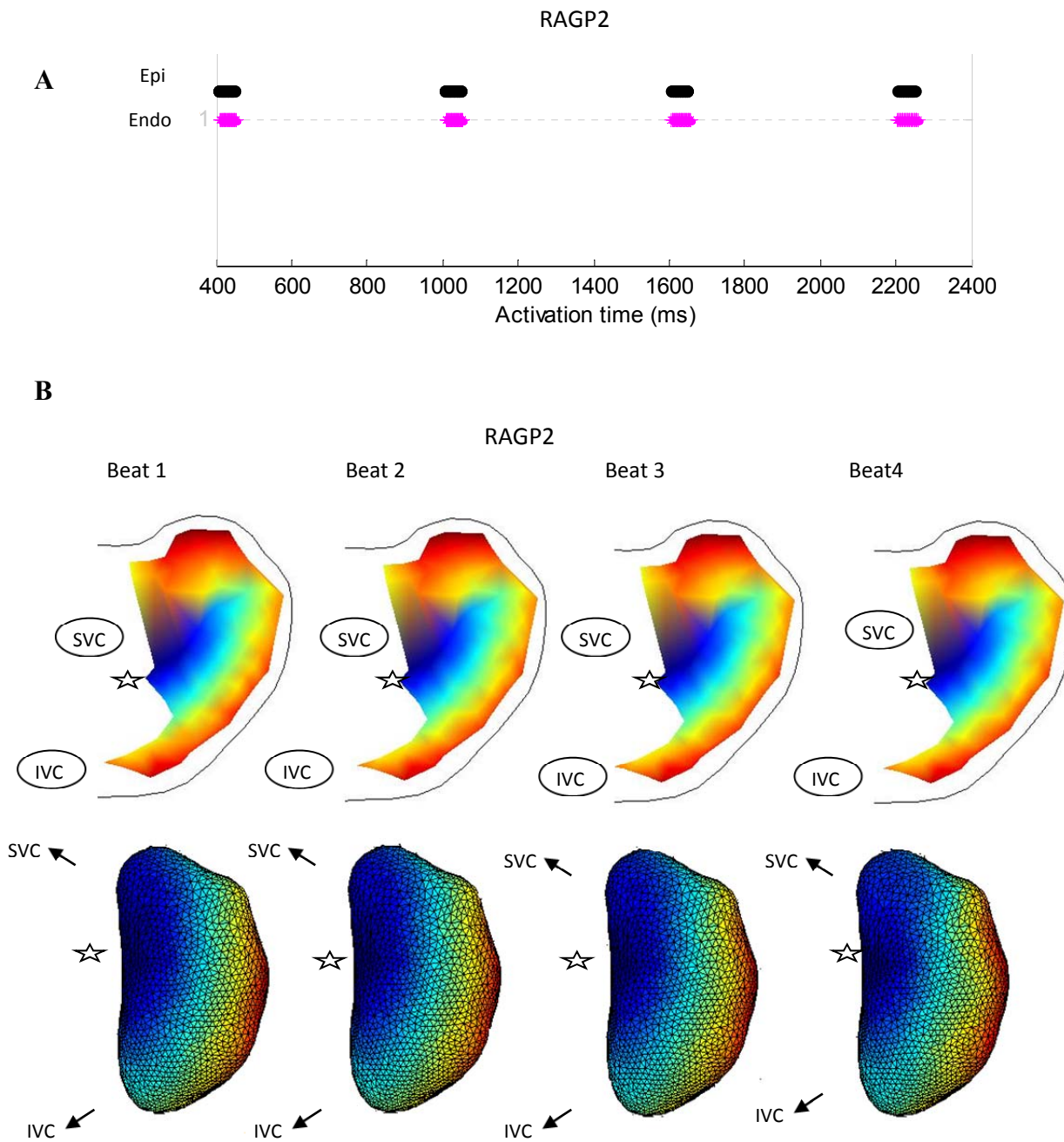
Figure 1.23- Simulated activation times; (A) Activation times are plotted for one experiment to notice the correspondence between the beats. (B) Activation times are mapped for the same beats. Anatomical locations are shown by the stars and arrows. SVC superior vena cava; IVC inferior vena cava, RAGP right atrium ganglionic plexi (catheter location).

1.8.2 Area under the atrial T wave

Spatial repolarization changes can be measured by computing the area under the repolarization

waveform. For atrial waves, it is known as area under the atrial T wave or ATa. ATa is a marker

of arrhythmogenic repolarization gradient. We computed ATa by integration over a defined

distance start from 40 ms after the activation time, as shown in figure 1.24.The effect of stimulation of efferent autonomic neural elements on the atria has been studied by the area of QRST deflections to detect regional changes in atrial electrical activity[82]. Page et al. introduced ATa to identify the different spatial regions affected by specific nerve stimulation. The spatial distribution of repolarization changes displayed heterogeneity in atrial electrical response to autonomic nervous system stimulation[19,82].

Cardinal *et al.* induced tachyarrhythmias by mediastinal nerve stimulation to point out the relation between the origin of the beat immediately preceding tachyarrhythmias onset and spatially concordant sites of neurogenically induced repolarization changes using epicardial and non-contact endocardial mapping. They also showed the role of spatial heterogeneity of atrial repolarization properties in tachyarrhythmias initiation. Based on their results, further information about arrhythmias could be extracted by gaining insights into the electrophysiological markers related to repolarization properties in the atria[83].
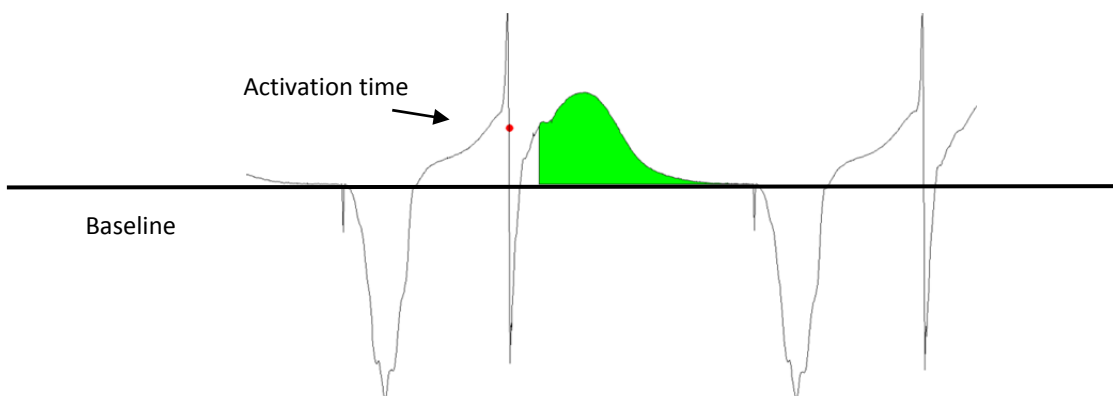
Figure 1.24- The area under the atrial T wave; ATa is shown by green color.

1.8.2.1 Correction of the baseline for ATa calculation

One of the difficulties for ATa calculation was possible (low frequency and typically small amplitude in our data) baseline wandering. We addressed this problem by detecting the last point of the integration and shifting it to zero for each beat in all 103 epicardial signals and 2048 endocardial signals (figure 1.25).
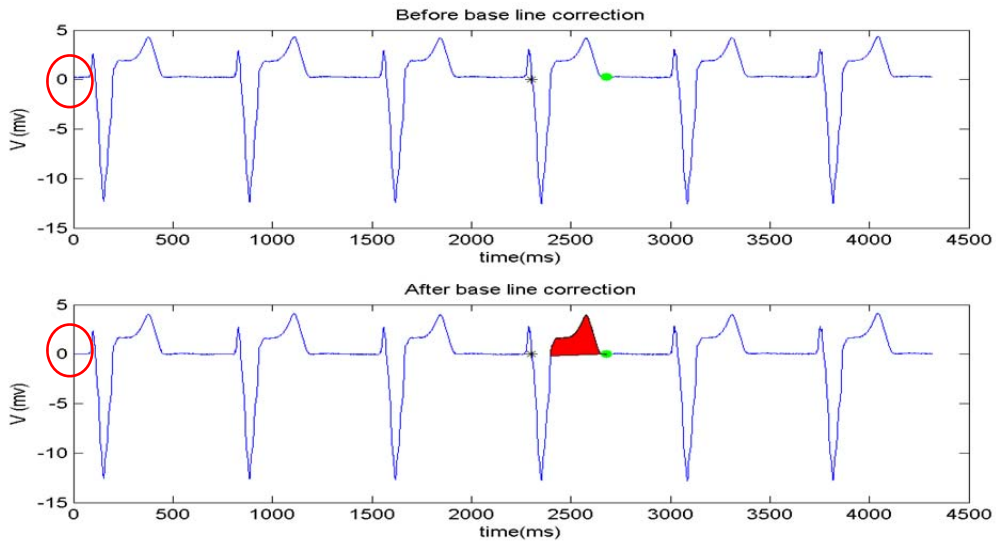
Figure 1.25- Baseline correction for computation of ATa (Experimental signals).

2   Article

Simultaneous epicardial and noncontact endocardial mapping of the canine right atrium: simulation and experiment

Sepideh Sabouri,[1,2] Elhacene Matene,[1,2] Alain Vinet,[1,2] Louis-Philippe Richer,[3]
René Cardinal,[1,4] J. Andrew Armour,[5] Pierre Pagé,[2,6] Teresa Kus,[1,4] and Vincent Jacquemet[1,2]

[1] Département de Physiologie, Université de Montréal, Montréal (QC) H3C 3J7, Canada;
[2] Centre de Recherche, Hôpital du Sacré-Coeur de Montréal, Montréal (QC) H4J 1C5, Canada;
[3] Conseil National de Recherche Canada, Montréal (QC) H4P 2R2, Canada; [4] Département de Pharmacologie, Université de Montréal, Montréal (QC) H3C 3J7, Canada; [5] Department of Pharmacology, East Tennessee State University, Johnson City, TN 37614, USA. [6] Département de Chirurgie, Université de Montréal, Montréal (QC) H3C 3J7, Canada

LPR, RC, JAA, PP and TK designed and performed the experiments. VJ developed the computer model. EM designed and ran the simulations. SS, AV and VJ designed the analysis methods. SS developed and implemented the electrogram processing toolbox and analyzed both the experimental and simulated data. SS and VJ prepared the figures and wrote the manuscript. All authors read the manuscript and gave suggestions.

2.1 Abstract

Epicardial high-density electrical mapping is a well-established experimental instrument to monitor *in vivo* the activity of the atria in response to pacing, remodeling, arrhythmias and modulation of the autonomic nervous system. In regions that are not accessible by epicardial mapping, noncontact endocardial mapping performed through a balloon catheter may provide a more comprehensive description of atrial activity. We developed a computer model of the canine right atrium to compare epicardial and noncontact endocardial mapping. The model was derived from an experiment in which electroanatomical reconstruction, epicardial mapping (103 electrodes), noncontact endocardial mapping (2048 virtual electrodes computed from a 64-channel balloon catheter), and direct-contact endocardial catheter recordings were simultaneously performed in a dog. The recording system was simulated in the computer model. For simulations and experiments (after atrio-ventricular node suppression), activation maps were computed during sinus rhythm. Repolarization was assessed by measuring the area under the atrial T wave (ATa), a marker of repolarization gradients. Results showed an epicardial-endocardial correlation coefficient of 0.8 (experiment) and 0.96 (simulation) between activation times, and a correlation coefficient of 0.57 (experiment) and 0.92 (simulation) between ATa values. Noncontact mapping appears to be a valuable experimental device to retrieve information outside the regions covered by epicardial recording plaques.

2.2 Introduction

Despite decades of investigations, many questions related to the mechanisms underlying the initiation and maintenance of atrial fibrillation remain open.[84] The origin of atrial fibrillation may be neurogenic (the role of the intrinsic cardiac nervous system is critical in this case), myogenic (related to abnormalities or remodeling in the heart muscle), or due to a combination of both.[85]

Animal models have been developed to investigate the relation between atrial fibrillation and the autonomic nervous system.[86] In these models, atrial tachyarrhythmias could be induced by electrically stimulating the vagosympathetic trunks in the neck[87] or mediastinal nerves.[88,89] Heterogeneity of repolarization was created locally in various atrial areas depending on which nerve was stimulated. Tachyarrhythmia beats typically originated from areas of increased repolarization heterogeneity.

The area under the atrial repolarization wave (ATa) in unipolar electrograms has been proposed as a marker of neurogenically-induced repolarization gradients.[90] The importance and spatial distribution of the influence of the autonomic nervous system on atrial repolarization has been demonstrated by measuring ATa in epicardial mapping data.[91] However, anatomical landmarks (fat pads, veins and arteries) caused obstruction to epicardial plaque placement, leaving relevant regions (e.g. septum) unmapped. To circumvent that problem, the use of noncontact endocardial mapping has been proposed.[91] Noncontact mapping[92,93] is a clinical device that computes virtual endocardial electrograms from a multielectrode array (balloon catheter) inserted in the atrium. This tool has been applied to assess reentrant circuits[49-51] and focal activity.[36] Activation and isopotential maps derived from virtual endocardial electrograms have been successfully compared to direct-contact mapping.[94,95] Simulation tools for noncontact mapping have been developed.[96] However, atrial repolarization waves and ATa in noncontact mapping has not been investigated yet.

The aim of this paper is to evaluate the use of noncontact mapping for extracting activation times and ATa values. Dog experiments and a computer model of the canine right atrium were combined to address this question. Simultaneous epicardial and noncontact endocardial mapping were compared in their ability to describe atrial depolarization and repolarization.

2.3 Material and methods

2.3.1 Animal preparation

A large mongrel dog (about 35 kg) was anesthetized by sodium thiopental and maintained under positive pressure ventilation. After bilateral open chest surgery to expose the heart, anesthetic was changed to α-chloralose. Atrioventricular blockade was performed by formaldehyde injection to dissociate atrial and ventricular electrical activity, as in Armour *et al.*[91] The right ventricle was electrically stimulated at 82 bpm to assure sufficient cardiac output. The atria were in sinus rhythm during the whole experiment. This study was approved by the ethical committee of the Hôpital du Sacré-Coeur de Montréal.

2.3.2 Experimental recording system

Two silicone plaques comprising 103 epicardial unipolar recording contacts were placed (1) in the right atrial free wall and lateral right atrial appendage (79 channels), and (2) in the Bachmann's bundle and adjacent base of the medial atrial appendage (24 channels).[91]The electrodes were connected to a multi-channel recording system (EDI 12/256, Institut de génie biomédical, École Polytechnique de Montréal). Signals were band-pass filtered (0.05-450 Hz) and digitized with a sampling rate of 1 kHz.

In parallel, a noncontact, endocardial balloon catheter (EnSite 3000 Multi Electrode Array with 64 channels; St Jude Medical Inc., St Paul, MN) was inserted in the right atrium. This device solves an inverse problem (see below) to compute endocardial electrograms at 2048 sites on a virtual closed surface representing the endocardium based on the potential at the 64 electrodes of the balloon.[41] This procedure requires reconstructing the endocardial geometry using a catheter localization system (EnSite NavX electroanatomical navigation system). Reconstruction of atrial geometry is shown in Fig. 2-1A for the dog considered in this study. The acquisition system

outputs 2048 (virtual) endocardial electrograms as well as 3-lead ECG at a sampling rate of 1.2 kHz.

A second catheter in the right atrium served to measure direct-contact endocardial bipolar electrograms. This catheter, also localized and tracked by the system, was moved to record signals at 7 different locations (> 5 sec stable recording at each location) near the superior vena cava, the right atrium ganglionated plexus, the inter-atrial bundles and the coronary sinus (stars in Fig. 2-1A).

Epi- and endocardial signals were simultaneously recorded using a separate digital acquisition system. To enable their synchronization, both systems had a "clock" input channel connected to a manually-driven tick generator.
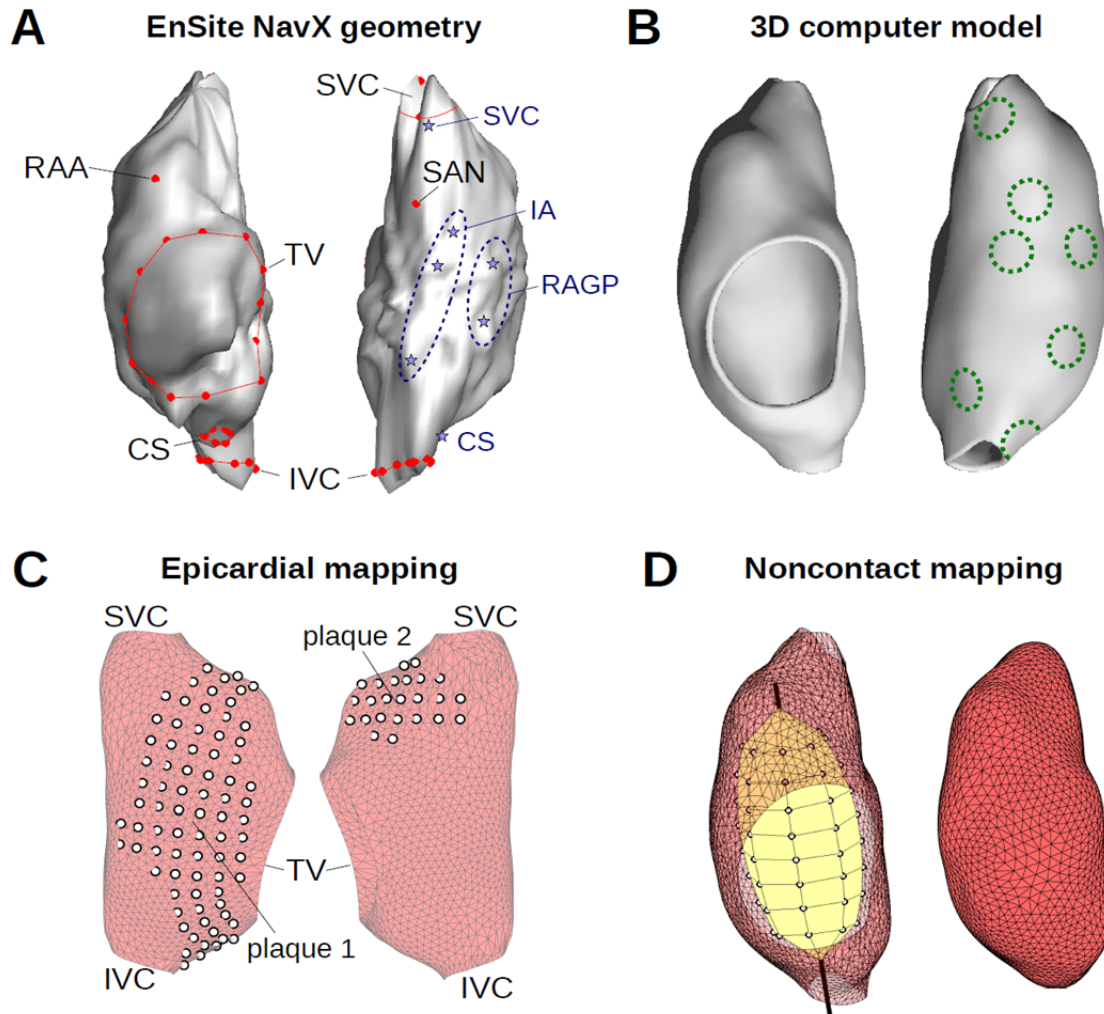
Figure 2.1- Right atrium geometry and electrode configuration. (A) Endocardial surface of a canine right atrium as reconstructed by the EnSite NavX system (*left side*: anterior view; *right side*: posterior view). Anatomical features identified by the catheter localization system are shown in red. Blue stars represent recording sites of the direct-contact endocardial catheter (B) 3D geometrical model (same views as panel A) of the right atrium after processing. Dashed circles represent the location of heterogeneity regions, shown here with a radius of 3 mm. (C) Epicardial electrode position for the two plaques in the computer model. (D) *Left side*: Balloon catheter with its 64 electrode. *Right side*: closed endocardial surface used for the inverse problem. RAA: right atrium appendage; SVC: superior vena cava; IVC: inferior vena cava; TV: tricuspid valve; CS: coronary sinus; SAN: sino-atrial node; RAGP: right atrium ganglionated plexus; IA: inter-atrial bundles.

2.3.3 Simulation of electrical propagation in the right atrium

The geometry extracted by the Ensite NavX system (Fig. 2-1A) formed the basis for constructing a 3D model of the canine right atrium. The triangulated surface was processed and smoothed

using VRMesh (VirtualGrid, Bellevue City, WA). Holes corresponding to the superior and inferior vena cava and to the tricuspid valve were created based on several points around their circumference identified using the catheter localization system (Fig. 2-1A). A thin-walled 3D cubic mesh (wall thickness: 1.75 mm; spatial resolution 0.25 mm; see Fig. 2-1B) was generated from the resulting triangulated surface as in our previous works.[97] Fiber orientation was specified following a rule-based approach.[98] There was no attempt to reproduce fine anatomical details and the trabecular structure of the right atrium (terminal crest and pectinate muscles) since no preparation-specific information was available for these anatomical features. Due to the limited spatial resolution of the NavX system, the details of the right atrium appendage anatomy were only grossly incorporated, as in older models.[8]

Electrical propagation was simulated by solving the monodomain equation[99] in the cubic mesh using finite difference methods.[100] Explicit time integration with a time step of 20 µs was used. Membrane kinetics was described by the Ramirez *et al.* model of canine atrial cell.[101,102] Effective tissue conductivity was 12 mS/cm (longitudinal), anisotropy ratio was 3:1, and membrane surface-to-volume ratio was 2000 cm^{-1}. Sinus rhythm propagation was elicited by injecting intracellular current at the anatomical location corresponding to the sino-atrial node (or more precisely to the focal point of activation) as identified using the catheter localization system (Fig. 2-1A).

To introduce repolarization heterogeneity in a way that replicates the Kneller *et al.* model of cholinergic atrial arrhythmia,[101] we created circular zones of heterogeneity in membrane properties (Fig. 2-1B). Similarly to Vigmond *et al.*,[71] zone radius was varied between 2 and 5 mm. In these zones (one at a time), acetylcholine (ACh) concentration was set to 0.03 µM based

on Kneller et al.[101] The resulting increase in ACh-dependent K+ current significantly shortened action potential durations in the zone, thus creating repolarization gradients.[71]

For each substrate (control + 7 zone locations × 3 zone radius = 22 simulations), sinus rhythm with a stable cycle length of 600 ms was simulated (experimentally-measured cycle length was 595±9 ms at baseline). Simulations were run until steady-state was reached, as determined by convergence of action potential durations (beat-to-beat variation < 1%). Analysis was performed on the last simulated beat.

2.3.4 Simulation of epicardial electrograms

Epicardial mapping ("plaques") was simulated using the same tools as in Jacquemet et al.[103] Two plaques were used, as in the experiment: one in the right atrium free wall and one between Bachmann's bundle and the appendage. Electrode configuration reproducing each experimental plaque was projected on the atrial epicardial surface on the basis of three manually-positioned control points (two electrodes at the extremities and one at the center of the plaque). The configuration is shown in Fig. 2-1C.

Electric potential at each of the 103 unipolar electrodes was computed using the current source approximation as in previous works.[19,103] In this framework assuming an infinite uniform volume conductor, the potential φ of an electrode located at $\mathbf{x}$ is given by

$$\varphi(\mathbf{x},t) = \frac{1}{4\pi\sigma_o} \int_{Vmyo} \frac{I_m(\mathbf{y},t)}{\|\mathbf{x}-\mathbf{y}\|} d\mathbf{y} \qquad (1)$$

where is σ_o the extracellular conductivity, I_m is the transmembrane current computed from the time course of the membrane potential in all simulated cardiac cells, and *Vmyo* is the integration domain (myocardium).[99] The same formula (1) was used to compute potentials in the endocardium and in the blood cavity (see below).

2.3.5 Simulation of noncontact endocardial electrograms

Since the EnSite software is proprietary, the noncontact mapping system was simulated using not exactly the same method, but a conceptually similar one based on Harley *et al.*[104] In these approaches, the atrial geometry is specified by a closed surface S near the endocardium and whose interior V contains only blood. The surface S used by the EnSite software for the experiments is displayed in Fig. 2-1A; the one used for the simulations is shown on the right side of Fig. 2-1D. The 64 electrodes of the Ensite Array Catheter are located at x_i, i = 1 to 64, all inside the surface S (Fig. 2-1D, left side). Potentials at these 64 electrodes were computed using Eq. (1). Assuming homogeneity and isotropy of blood conductive properties and neglecting the effect of the catheter on volume conduction, the electric potential φ satisfies the Laplace equation $\Delta\varphi = 0$ in V.

The effect of the catheter was ignored in order to be consistent with the assumptions of electrogram computation [Eq. (1)]. In more sophisticated models, the interior of the catheter is assumed to be an insulator, resulting in a no-flux boundary condition on the surface of the balloon catheter[103].

Because of the uniqueness of the solution to the Laplace equation with Dirichlet boundary conditions, the values of φ on S determine the value of φ at x_i, denoted by φ_i^c (c stands for catheter). An explicit formula can be derived from potential theory. From the Green's second identity, if x is in the interior of V, then[104]

$$\varphi(\mathbf{x}) = \frac{1}{4\pi} \oint_S \left(\frac{1}{r}\nabla\varphi - \varphi\nabla\frac{1}{r} \right) d\mathbf{S} = -\frac{1}{4\pi} \oint_S \frac{1}{r} E^e \, dS - \frac{1}{4\pi} \oint_S \varphi \, d\Omega, \qquad (2)$$

where r is the distance between $\mathbf{x}$ and the surface element dS, E^e is the normal component of

$-\nabla\varphi$ with respect to the surface S (the index e stands for endocardium), and $d\Omega(\mathbf{y},\mathbf{x}) = \nabla(1/r)d\mathbf{S}(\mathbf{y})$ is the solid angle subtended at $\mathbf{x}$ by the element $d\mathbf{S}$ located at $\mathbf{y}$.[99]

In order to compute these integrals numerically, S is discretized as a triangulated surface with N nodes located at $\mathbf{y}_j$, $j = 1$ to N, where N is of the order of 2000. The field φ is approximated on the endocardium surface S using piecewise linear basis functions ψ_j:

$$\varphi(\mathbf{y}) = \sum_{j=1}^{N} \varphi_j^e \, \psi_j(\mathbf{y}), \tag{3}$$

where $\varphi_j^e = \varphi(\mathbf{y}_j)$. If the 64-by-$N$ matrices $\mathbf{O}^{ec}$ and $\mathbf{S}^{ec}$ are defined as:

$$O_{ij}^{ec} = \frac{1}{2\pi} \oint_S \frac{\psi_j(\mathbf{y})}{\|\mathbf{y}-\mathbf{x}_i\|} \, dS(\mathbf{y}) \quad \text{and} \quad S_{ij}^{ec} = -\frac{1}{2\pi} \oint_S \psi_j(\mathbf{y}) \, d\Omega(\mathbf{y},\mathbf{x}_i), \tag{4}$$

then (2) can be written as

$$\boldsymbol{\varphi}^c = -\frac{1}{2}\mathbf{O}^{ec}\mathbf{E}^e + \frac{1}{2}\mathbf{S}^{er}\boldsymbol{\varphi}^e . \tag{5}$$

Similarly, if $\mathbf{x}$ is on the boundary S, because of the singularity at $r = 0$,

$$\varphi(\mathbf{x}) = -\frac{1}{2\pi} \oint_S \frac{1}{r} E^e \, dS - \frac{1}{2\pi} \oint_S \varphi \, d\Omega , \tag{6}$$

and by defining the N-by-N matrices $\mathbf{O}^{ee}$ and $\mathbf{S}^{ee}$ as

$$O_{ij}^{ee} = \frac{1}{2\pi} \oint_S \frac{\psi_j(\mathbf{y})}{\|\mathbf{y}-\mathbf{y}_i\|} \, dS(\mathbf{y}) \quad \text{and} \quad S_{ij}^{ee} = -\frac{1}{2\pi} \oint_S \psi_j(\mathbf{y}) \, d\Omega(\mathbf{y},\mathbf{y}_i) , \tag{7}$$

the potential on the surface satisfies the equation

$$\boldsymbol{\varphi}^e = -\mathbf{O}^{ee}\mathbf{E}^e + \mathbf{S}^{ee}\boldsymbol{\varphi}^e . \tag{8}$$

After E^e is isolated in (8) and substituted in (5), the potential at the catheter electrodes is expressed as $\boldsymbol{\varphi}^c = \mathbf{T}^{ec}\boldsymbol{\varphi}^e$, where the 64-by-$N$ forward transfer matrix is given by

$$\mathbf{T}^{ec} = \frac{1}{2}\left(\mathbf{O}^{ec}\left(\mathbf{O}^{ee}\right)^{-1}\left(\mathbf{I} - \mathbf{S}^{ee}\right) + \mathbf{S}^{ec}\right), \tag{9}$$

where $\mathbf{I}$ is the identity matrix. Since the function ψ_j is linear on every triangle, the integrals from (4) and (7) are finite and can be computed analytically,[105,106] including in the presence of a singularity (*i.e.* when r = 0 in the integration domain). The auto-solid angle S_{ii}^{ee} is defined such that the sum of each row of $\mathbf{S}^{ee}$ gives 1.

To estimate the potential at the endocardium from the potential at the catheter electrodes, the forward transfer matrix needs to be inverted. Because the system is underdetermined, Tikhonov regularization[99] was used to compute the inverse transfer matrix $\mathbf{T}^{ce}$:

$$\mathbf{T}^{ce} = \left(\mathbf{T}^{ec^t}\mathbf{T}^{ec} + \lambda\mathbf{I}\right)^{-1}\mathbf{T}^{ec^t} \tag{10}$$

where λ is a positive regularization parameter. The parameter λ was set to $1.4 \cdot 10^{-5}$ based on a comparison between electrograms computed directly using Eq. (1) and those obtained by solving the inverse problem.

2.3.6 Processing of atrial electrograms

Atrial activation times were identified in both epi- and endocardial electrograms using a dedicated event detector based on signal derivative.[107] Activation maps were validated manually by visual inspection of electrogram waveforms and activation times. Noncontact mapping sometimes produced fractionated endocardial waveforms (double potentials due to solution of inverse problem which can oscillate wildly) that reduced the accuracy of detected activation times. To cope with that limitation, spatial filtering (Gaussian filter with a space constant of 5 mm) was applied to the resulting endocardial activation maps.

For each ventricular activation in the experimental signals, the onset of the Q wave and the offset of the T wave were identified manually on the ECG. For each atrial activation, the atrial activity

interval was defined as the time interval between the earliest atrial activation time and the latest atrial activation + 300 ms, assuming that atrial action potential durations were always shorter than 300 ms (which was *a posteriori* verified by inspecting the atrial T waves). Only atrial beats for which the atrial activity interval did not overlap with any QT interval were considered for subsequent analysis, in order to prevent the contamination of atrial signals by ventricular activity. This issue was not present in the simulated signals.

To quantify the local repolarization gradient, the area under the atrial T wave[19,90] (ATa) was computed. The (non-dimensional) ATa of an electrogram waveform $\varphi(t)$ was defined as:

$$ATa = \frac{1}{T_2 - T_1} \int_{T_1}^{T_2} d\tau \, \frac{\varphi(t_a + \tau) - \varphi(t_a + T_2)}{\sigma_\varphi}, \tag{11}$$

where t_a is the activation time and σ_φ is the standard deviation of the whole signal φ. The integration bounds T_1 and T_2 were initialized to 50 and 300 ms. Further manual validation was performed to ensure appropriate positioning of integration bounds. After minor manual adjustments (mostly for the lower bound), the interval length $T_2–T_1$ was respectively 256±20 ms and 254±16 ms in epi- and endocardial experimental signals. For simulated signals, the bounds were set to $T_1 = 35$ ms and $T_2 = 300$ ms. Normalization by interval length was aimed at providing a non-dimensional ATa. It did not significantly influence the results since interval length was essentially the same across all electrodes. Amplitude normalization compensated epi-endo and between-channels amplitude differences that may be generated by the inverse problem solver, and facilitated the comparison between simulations and experiments. Baseline correction applied in (11) assumed that the point at the upper integration bound was isoelectric (just after the end of atrial repolarization and before the next onset of the Q wave). Since the previous and next atrial beats were typically partially masked by ventricular activity no interpolation of the isoelectric line was possible.

2.3.7 Correspondence between epicardial and endocardial maps

One issue was to determine which endocardial electrode was closest to each epicardial electrode. In the computer model, this task was simply performed by identifying the endocardial electrode that minimized the Euclidian distance to the given epicardial electrode. In the experiment, the locations of epicardial electrodes in the EnSite endocardial coordinate system were not accurately known. The approximate location of some of the electrodes was however obtained using the catheter localization system.

The epi-endo correspondence was reconstructed iteratively. The grid of electrodes (plaques) was created based on three control points (like for the simulation of epicardial mapping, see above). The location of these three points was initialized using *a priori* knowledge about plaque placement. Their positions were then adjusted by random search within circular regions of diameter 5 mm around each initial control point position. The optimization criterion was the root mean squared (RMS) difference between activation times in the epicardial map and at the corresponding electrodes of the endocardial map, summed up over three carefully-validated beats. Since anatomical reconstruction of the appendage was not accurate, electrodes located in the appendage were excluded in the computation of the optimization criterion.

2.4 Results

2.4.1 Activation maps

During the experiment, the RR interval was 733±2 ms (ventricular pacing) and the QT interval was 353±22 ms. As a result, there were sequences of 380-ms intervals free of ventricular activity, while atrial depolarization and repolarization always lasted less than 350 ms. In total, 12 atrial beats were found in these intervals free of ventricular activity. At least one suitable beat was identified for each of the 7 recording sites of the endocardial catheter.

Figures 2-2A and B show an example of simultaneous epicardial and endocardial mapping. The location of epicardial electrodes on the endocardial surface (white dots in Fig. 2-2A) were obtained by optimization of the correspondence between epi- and endocardial map (Fig. 2-2C). The overall epi- and endocardial activation patterns were consistent. The RMS difference in activation time was 10 ms and the correlation coefficient was 0.8. The main inconsistency between epi- and endocardial mapping was found in the appendage, a region that is distant from the balloon catheter and at the same time poorly geometrically represented for the inverse problem. Note that the sinus beat originates from a focal point located outside the epicardial plaques.

In the computer model, exactly-known electrode location and geometry improved the consistency of the results. The endocardial activation map (Fig. 2-2D) was quantitatively similar to the epicardial map (Fig. 2-2E). Epi- and endocardial times (Fig. 2-2F) had a correlation coefficient of 0.96 and an RMS difference of 3.5 ms. The repolarization heterogeneities considered (changes in ACh concentration) had essentially no effect on the activation map at 100 bpm (maximum difference < 0.8 ms).

With the exception of the appendage region, the computer model qualitatively reproduced experimental epi- and endocardial activation. Simulated and experimental epicardial maps (18 appendage data points excluded) had a correlation coefficient of 0.82 with an RMS difference of 6.8 ms (respectively 0.7 and 8.5 ms with all data points included). Since the computer model was derived from the experimental endocardial surface, endocardial activation could also be easily compared (data points in the valve and veins were excluded). Simulated and experimental endocardial activation times had a correlation coefficient of 0.91 with an RMS difference of 11 ms.

Figure 2.2- Endo- and epicardial activation maps in the experiment (A-C) and in the computer model (D-F). (A) Color-coded experimental endocardial activation map. White dots represent epicardial electrode positions. The white star denotes the earliest activation point. (B) Experimental epicardial activation map for the same atrial beat. (C) Epi- vs endocardial experimental activation times, along with the linear regression curve (dashed black line), for the three beats (each shown with a different color) that served to identify epicardial plaque location. (D) Simulated endocardial activation map in control. (E) Simulated epicardial activation map. (F) Epi- vs endocardial simulated activation times. SVC: superior vena cava; IVC: inferior vena cava; RAA: right atrium appendage; BB: Bachmann's bundle; RAGP: right atrium ganglionated plexus.

2.4.2 Morphology of bipolar electrograms

Direct-contact bipolar electrograms (Fig. 2-3, first row) were recorded at the 7 endocardial sites as shown in Fig. 2-1A. Since noncontact endocardial electrograms were unipolar, noncontact bipolar electrograms were reconstructed by computing the difference between noncontact unipolar electrograms measured at two locations in the vicinity (<5 mm) of the bipolar recording

site (Fig. 2-3, second row). Because bipolar waveform depends on the unknown orientation of the bipolar electrode, the location of these two sites were adjusted to better match direct-contact recording. The correlation coefficient between contact and noncontact waveforms ranged from 0.8 to 0.95, except near the coronary sinus where the value was lower.

In the computer model, bipolar electrograms were also computed as the difference between unipolar electrograms at two close sites. Dipole orientation was selected to generate the same types of waveform morphology observed in the experiment (Fig. 2-3, third row). Noncontact bipolar electrograms (Fig. 2-3, fourth row) were computed as the difference between two noncontact unipolar electrograms measured at exactly the same location as the direct-contact unipolar electrograms. Correlation coefficient between contact and noncontact waveforms ranged from 0.62 to 0.92, except in the coronary sinus. These values are sometimes lower than in the experimental data because we have not allowed the independent optimization of noncontact electrode positions with respect to the catheter electrode.
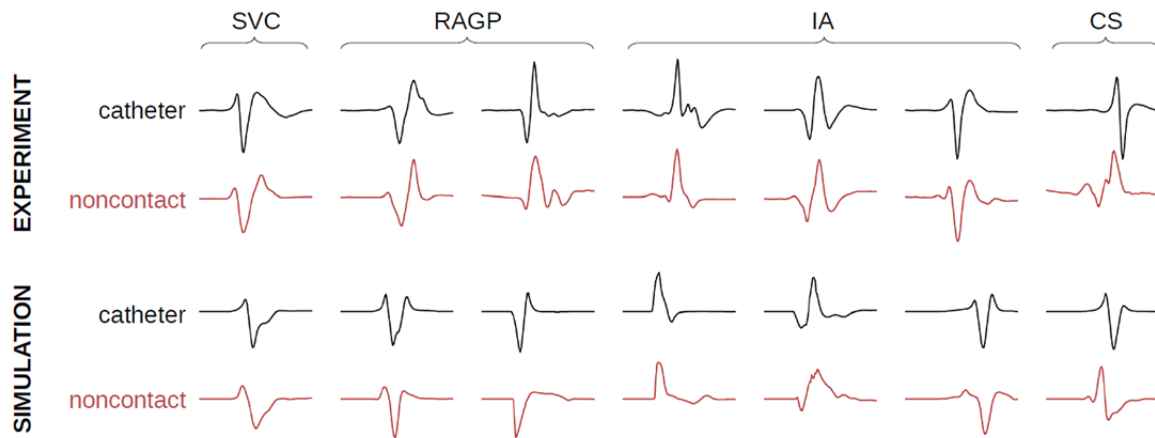
Figure 2.3- Morphology of direct-contact (catheter) and non-contact bipolar electrograms for 7 recording sites in the experiment and in the computer model. SVC: superior vena cava; RAGP: right atrium ganglionated plexus; IA: inter-atrial bundles; CS: coronary sinus.

2.4.3 Area under the atrial T wave

The ATa provides a quantitative measure to assess atrial repolarization in experimental electrical recordings. Figure 2-4 illustrates the range of atrial T wave morphologies observed in the experiments and in the simulations at corresponding epi- and endocardial sites. Simulated atrial T waves had significantly lower amplitude (similarly to Vigmond et al.[19]), suggesting that canine atria contain more intrinsic heterogeneities than the model. Despite some differences in epicardial and noncontact endocardial atrial T wave morphology (notably atrial T wave did not become negative in experimental noncontact signals), epi- and endocardial ATa measurements appears to be correlated in these examples.
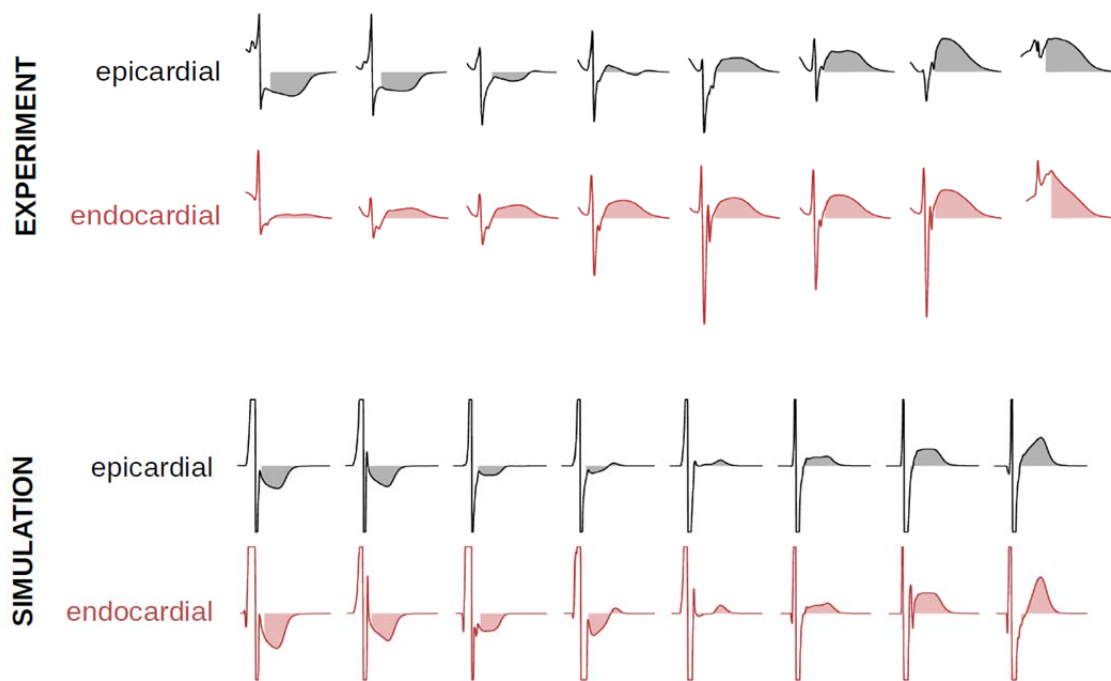
Figure 2.4- Examples of unipolar epicardial and noncontact endocardial electrograms measured at corresponding epi- and endocardial sites (both experimental and simulated). The area under the atrial T wave is displayed as a shaded area. Simulated signals are saturated to highlight their atrial T wave.

To further investigate this question, epi- and endocardial ATa maps were compared (Figs. 2-5A and B). The epi- and endocardial ATa patterns were found to be qualitatively comparable, except

in the right appendage where signals were less reliable. The correspondence between epi- and endocardial ATa is summarized in Fig. 2-5C for all electrodes and 12 beats. To facilitate the interpretation, data point density was estimated using a kernel-based method[108] (kde2d Matlab script implementation by Z. I. Botev, available on Matlab Central website) and displayed as contour lines. The correlation coefficient between epi- and endocardial ATa values was 0.57.

The same analysis was performed on simulated data. Note that there was no attempt to match experimental repolarization properties. Figures 2-5D and E show endo- and epicardial ATa maps for a simulated beat with a heterogeneity region of radius 3 mm around the white star in Fig. 2-5D. This region of increased repolarization gradients was characterized by higher ATa values. Epi- and endocardial ATa maps were consistent. The correlation coefficient between epi- and endocardial ATa values from the 22 simulations with different repolarization heterogeneity distributions was 0.92, as illustrated in Fig. 2-5F.
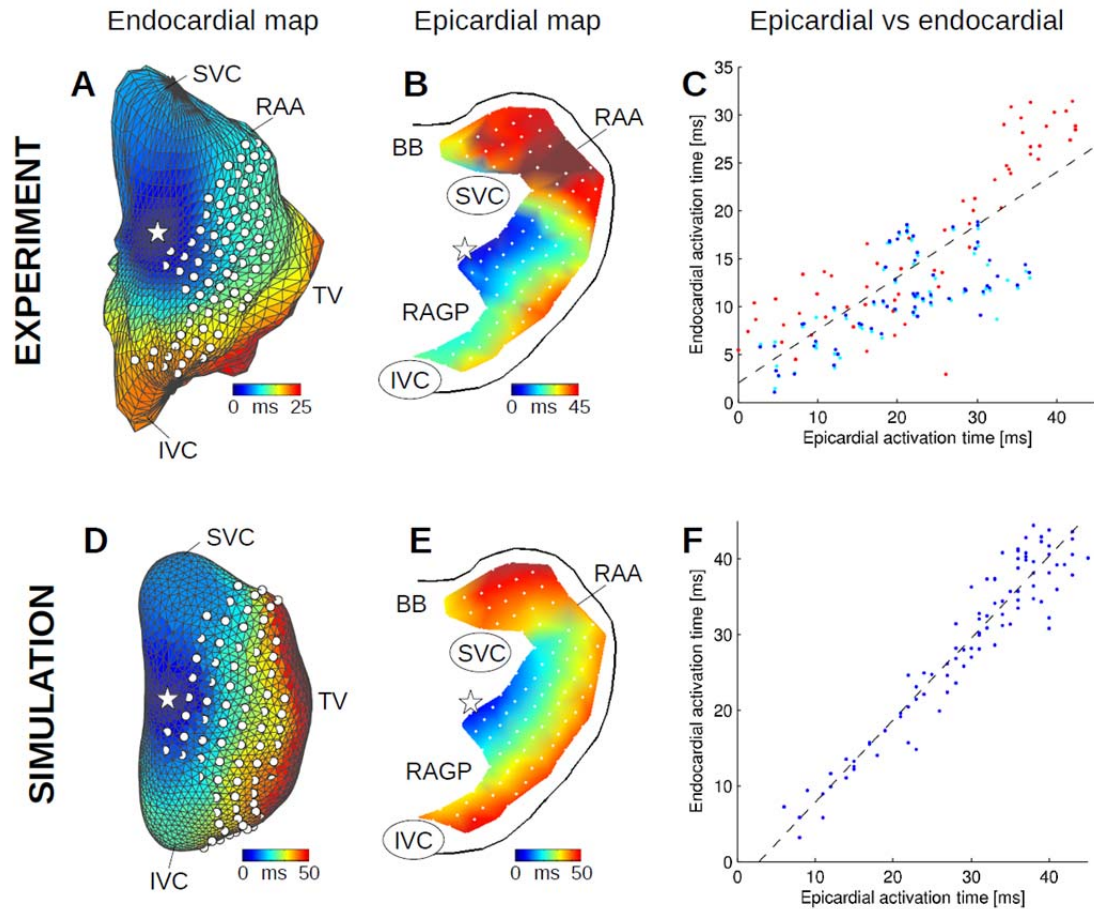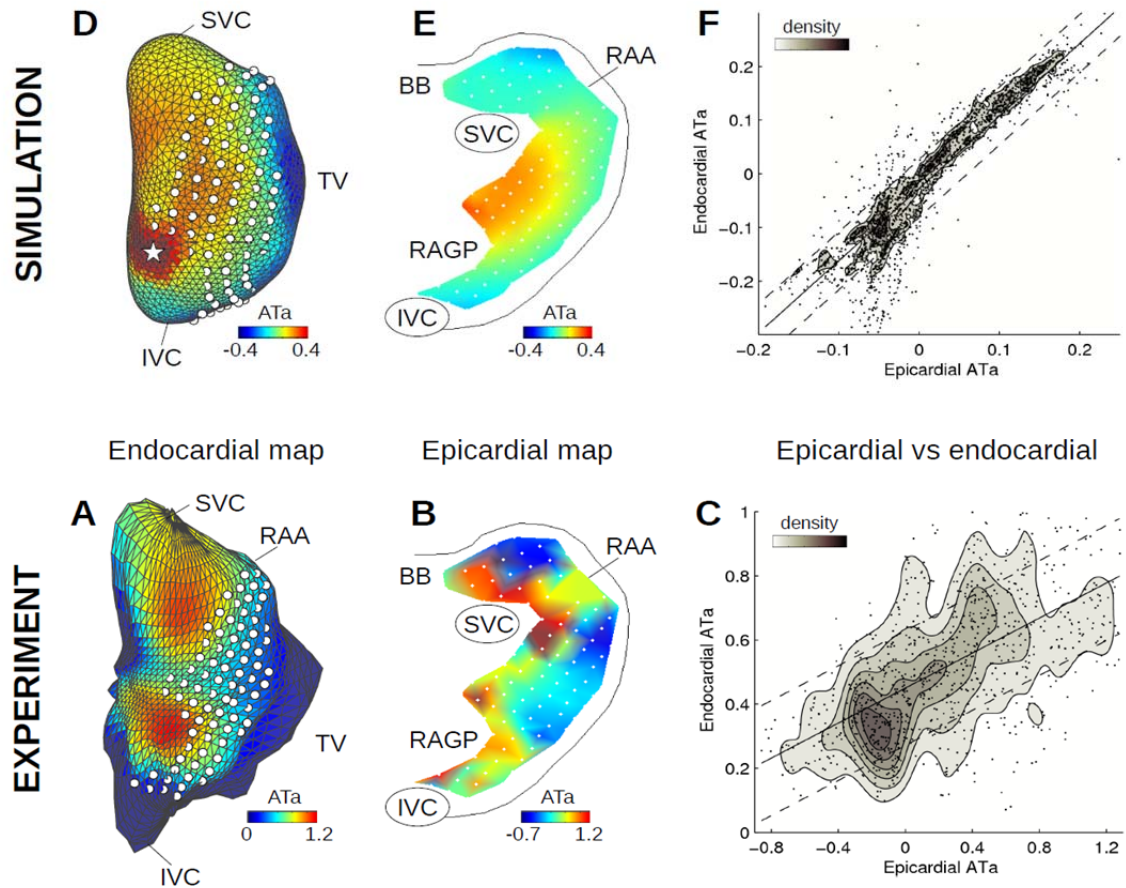
Figure 2.5- Endo- and epicardial ATa maps in the experiment (A-C) and in the computer model (D-F). (A) Color-coded experimental endocardial ATa map. White dots represent epicardial electrode positions. (B) Experimental epicardial ATa map for the same beat. (C) Epi- vs endocardial experimental ATa for all beats combined, along with the linear regression curve and 50% confidence interval. Data point density estimated by kernel-based method is displayed as contour lines. (D) Simulated endocardial ATa map in the presence of a repolarization heterogeneity with a radius of 3 mm around the white star. (E) Simulated epicardial ATa map for the same beat. (F) Epi- vs endocardial ATa for all simulations with different repolarization heterogeneity distributions. SVC: superior vena cava; IVC: inferior vena cava; RAA: right atrium appendage; BB: Bachmann's bundle; RAGP: right atrium ganglionated plexus.

2.4.4 Temporal changes in area under the atrial T wave

Experimental endocardial ATa maps were similar in the 12 analyzed beats. The correlation coefficient between any pair of them was always >0.9. The differences between ATa maps (separated by a few seconds or minutes) may reflect autonomic neural modulation.[91] To illustrate how endocardial ATa maps may be used to identify changes that occur outside the region

covered by epicardial mapping, Figs. 2-6A-C displays ATa maps for two beats as well as their difference (ΔATa). On the ΔATa map, regions where changes occur can be easily identified.

In the simulations (Figs. 2-6D-F), repolarization gradients were induced by increasing ACh concentration in a circular zone, which affected ATa values. In the control beat (Fig. 2-6D), spatial variations in ATa were observed due to small repolarization gradients created by wavefront curvature or collision (this effect was |ΔATa| < 0.04 in epicardial signals), and also due to distortions caused by the inverse problem. After subtraction, though, the pattern became clearer (Fig. 2-6F), thus enabling localization of the altered region. The distance between the center of the altered region and the maximum of the ΔATa map was < 5 mm for the 4 regions in the right atrium ganglionated plexus and the inter-atrial bundles (Fig. 2-1B), and < 9 mm for the 3 regions closest to the venae cavae. For the region near the superior vena cava, changes in repolarization were detectable only for a radius > 3 mm. Otherwise, the radius of the region did not significantly affect the results in the range of parameters considered.
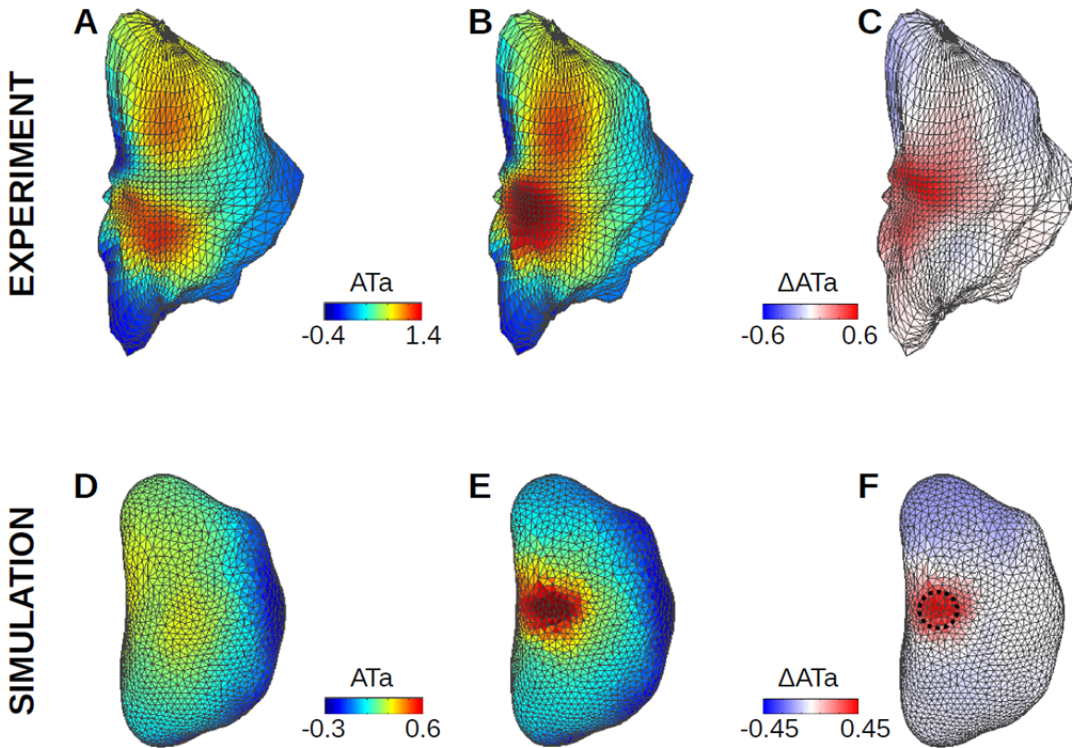
Figure 2.6- Endocardial ATa maps. (A) First experimental beat. (B) Another beat at a later time. (C) Difference between maps A and B. (D) Simulated ATa map during sinus rhythm in a uniform substrate. (E) Simulated ATa map with repolarization heterogeneity (3 mm radius in the right atrium ganglionated plexus; shown as a dashed circle). (F) Difference between maps D and E.

2.5 Discussion

This paper presents a computational framework to evaluate the potential of noncontact mapping as a complement to epicardial mapping for studying neurogenically-induced changes in activation pattern and repolarization gradients. The simulation results can be seen as a best-case scenario as compared to animal experiment. The heart is not mechanically beating and the electrodes stay at fixed, exactly known locations. In this situation, noncontact mapping was able to correctly represent both activation maps (depolarization, Fig. 2-2) and ATa maps (repolarization, Fig. 2-4), making it possible to identify and localize changes in repolarization properties (Fig. 2-6). In the control case with uniform membrane properties, ATa values derived

from noncontact mapping were overestimated in the region were the balloon catheter was closest (Fig. 2-6D, where tissue properties are uniform), suggesting that the inverse problem introduces distortions that are noticeable in the repolarization phase. These distortions were however considerably reduced on ΔATa maps (Fig. 2-6). Note that the numerical methods and the inverse problem procedure could be improved.[96] Our intent was not to overperform the commercial package EnSite, but rather to illustrate in a computer model the possible distortions that the inverse problem can create. Further development of the model including more detailed anatomical representation of the trabecular structure and intrinsic variations in membrane properties would influence the baseline ATa map and require the use of ΔATa maps to properly interpret the data.

To compare epi- and endocardial data in the experiment, a major obstacle was to associate each epicardial electrode to an endocardial channel. Here, an optimization scheme was used to position the grid on the atrial surface. More reliable information about this correspondence may further improve the correlation between epi- and endocardial data (Figs. 2-2 and 2-4). Because of heart motion and limited details in geometrical reconstruction (especially veins, valve and appendage), this correspondence may however not be perfectly accurate. On the other hand, when signals from the endocardial catheter and from noncontact endocardial channels at the same known location were compared, waveform morphology was relatively similar (Fig. 2-3), as reported in previous clinical and modeling works.[36,95,96]

The relevance of epicardial ATa measurements for the identification of regions responding to autonomic neural modulation has been demonstrated in canine experiments and in computer models. Occasionally, epicardial plaques failed to identify the origin of neurogenically-induced ectopic beat when it occurred outside the region covered by the plaques. The extension to

noncontact endocardial ATa would allow extracting information about regions that cannot be mapped on the epicardium. Results showed consistent ATa patterns in epi- and endocardial electrograms despite several limitations (Fig. 2-4). Noncontact endocardial signals, reconstructed from 64 electrodes, did not reproduce the full spectrum of atrial T wave morphologies observed in epicardial signals. For example, the ATa was always positive in noncontact signals, while many epicardial channels featured negative ATa values. Endocardial ATa maps were smoother, which facilitated the identification of regions with increased ATa (as in Fig. 2-6) but did not reproduce the large differences in ATa sometimes observed between neighboring epicardial electrodes. Although used here as reference, epicardial mapping has also its limitations regarding ATa measurement, notably in the appendage where the tissue had to be "flattened" to suture the plaques. Discrepancies between epi- and endocardial ATa could be caused by distortions in epicardial signals. In addition, there may be actual differences in epi- vs endocardial electrical activity due to complex (micro-) structures within the atrial wall.

The application of noncontact mapping to animal experiments has been so far very rare. The system has been designed for clinical setting. As a result, the atrial chambers need to be large enough to insert the balloon catheter (the balloon may not be maximally expanded if necessary), as is the case with large dogs. A more severe limitation (as in most unipolar recordings) is the contamination by ventricular activity. Atrio-ventricular node suppression and beat selection enabled us to extract atrial beats free of ventricular activity. In order to monitor ATa on a beat to beat basis, efficient QRST cancellation algorithms dedicated to atrial electrograms need to be developed. This would be a prerequisite for clinical applications.

Overall, noncontact mapping provides a complementary tool to achieve a more complete description of atrial electrical activity in canine experiments. Despite distance (balloon-atrial

wall) and dimension reduction (64 electrodes), some information about atrial repolarization remains present in noncontact signals. Further validation in the context of nerve stimulation (neurogenically-induced changes in repolarization) would reveal the ability of this technique to examine the activity preceding the onset of atrial arrhythmias.

2.6 Acknowledgments

3 Discussion

Our aim was to combine epicardial contact mapping and endocardial non-contact mapping to investigate the possibility of extracting additional information about atrial repolarization heterogeneity in a dog. Contact mapping consisted of 103 unipolar electrodes located in the right atrium. Non-contact mapping was performed using the EnSite multielectrode array (balloon catheter with 64 electrodes). Contact and non-contact electrograms were also simulated in an electro-anatomical computer model of canine right atrium. We compared non-contact endocardial mapping with contact epicardial mapping to evaluate the use of non-contact mapping in experiments and simulations. In order to gain information about both depolarization and repolarization, activation times and ATa parameter values were extracted from epicardial and non-contact endocardial electrograms for both experiments and simulations. Correlation coefficients were computed for both mapping systems in terms of the area under the atrial T wave (ATa) as well as activation times. They were well correlated in the experimental and simulated electrograms.

Endocardial non-contact mapping can provide access to the regions that are not accessible by epicardial mapping. This mapping system may provide more information about reentry circuit and origin of atrial fibrillation. Furthermore, more information about atrial arrhythmias may be obtained by looking at non-contact mapping data during sinus beats preceding neurogenically induced atrial fibrillation. A combination of epicardial mapping and endocardial mapping system appears to be an excellent option to explore heart diseases.

We concluded that non-contact mapping is a complement to epicardial mapping since it can display cardiac potentials as a 3D color coded map of the entire cardiac chamber. It could also provide more information about heart electrophysiology during sinus rhythm or arrhythmias such

as atrial fibrillation since noncontact virtual electrograms are simultaneously available at all locations throughout the endocardium. Consequently, this technology has a potentially broad utility in the diagnosis and treatment of a wide range of cardiac arrhythmias and could possibly be considered as a first line approach for treatments of nonsustained, complex, and unknown arrhythmias.

The activation time and ATa can be computed in signals captured during neurogenically induced repolarization gradient-leading to AF as shown in figure 3.1- and mapped for both mapping systems. This would allow us to investigate about initiation of AF in dog experiments. The activation and ATa maps would help us to address questions such as where does AF most frequently occur? How is it initiated?   Does it take a long time to start AF after tachyarrhythmias? Can we extract the features of beats before AF initiation in order to predict AF occurrence or location of reentry circuits?

We listed the works in the following paragraphs that could be done to address these questions, as well as some preliminary data for the sake of illustration.

3.1 Activation time maps in the presence of neurogenically induced repolarization gradient

The involvement of different neuronal elements in the genesis of neurogenically induced atrial fibrillation has already been described by Armour at al[81]. Subsequently, electrophysiological mapping may give us insights about the effect of each neuronal element on onset of atrial fibrillation. In order to have better understanding of loci initiating AF for treatment purposes such as ablations, we suggest that sites of origin of initiating beat- the onset of atrial fibrillation-can be identified by applying these two mapping systems as shown in figures 3.1 and 3.2.

In figure 3.1, the earliest activation starts from the superior portion of right atrium or SVC in the basal beats, and terminates in the IVC and RAA. The earliest activation time in the second group of the beats initiates from inferior right atrial regions and stops in the RAA. The initiation point has completely changed in the last beat that occurs in IVC and terminates in SVC, indicating heart rhythm irregularity. The same changes have been seen for the next group till AF.
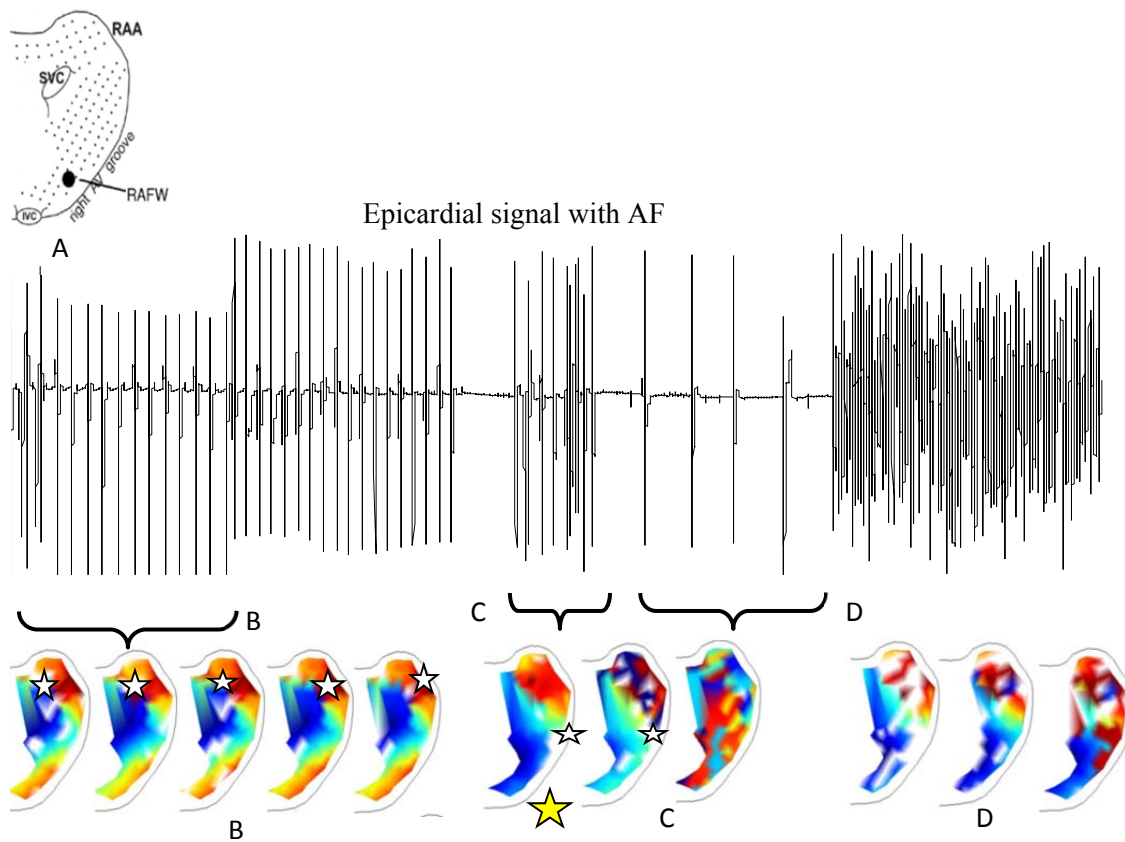
Figure 3.1- The upper diagram is a schematic view of 2 plaques carrying 103 unipolar recording contacts distributed over the entire right atrial epicardial surface (SVC, IVC –superior and inferior vena cava; RAA- right atrial appendage; RAFW- right atrial free wall). (A) The unipolar epicardial electrogram demonstrates responses of right atrium to electrical stimuli which were delivered to vagal nerve. It illustrates the sinus rhythm followed by tachycardia, bradycardia, and atrial fibrillation. Epicardial maps demonstrate activation pattern of selected beats. Beat 1 to 5 (group B) are basal beats or sinus rhythms in which the earliest epicardial activations (shown by asterisks) are started from SVC- SA node located in the SVC- then continued toward inferior portion of right atrium, and finally terminated in IVC and RAA. Group C (tachycardia), the earliest epicardial activations start from inferior right atrial regions i.e. the areas where the earliest activation shifted to the locations in IVC; and terminated at RAA which are indicated as irregularities in the heart's electrical activity pathways. It can be seen that the electrical activities are completely erratic in the last beat of this group. (D) Finally, the latter beats are bradycardia

before AF where earliest activations were shifted toward RAFW. The last map is atrial fibrillation which is difficult to interpret due to presence of multiple breakthrough areas.

In the figure 3.2, the earliest activation time starts in the inferior region of the SVC and goes to the IVC and RAFW which indicates changing in anatomical location of earliest pacemaker activity during neurogenically induced atrial fibrillation.
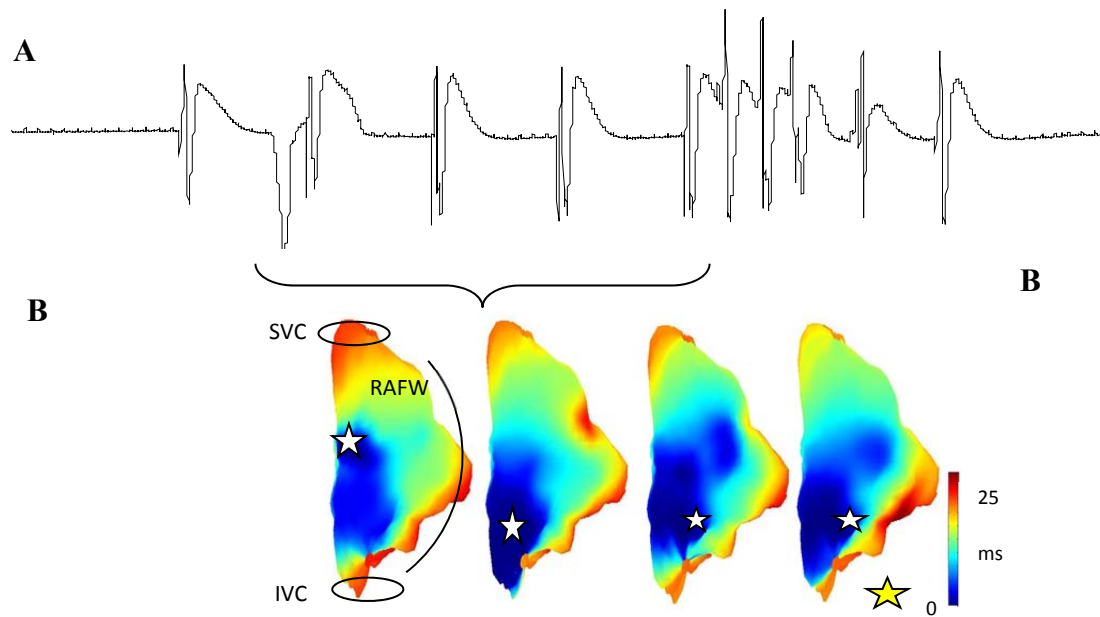
Figure 3.2- (A) The unipolar endocardial electrograms of the same case as the previous figure. AF started after 4 beats. (B) The earliest endocardial activation, shown by asterisks for the 4 beats, is caudally shifted from superior portion toward inferior portion of the right atrium. Atrial beat started from the IVC toward SVC instead of starting from the SVC. The origin of the activation is developed towards the RAFW in the last two beats.

Consequently, for the beat that led to onset of AF, the earliest activation time moved within the right atrium as compared to the basal beats in the two mapping systems (yellow asterisks).

3.2   SA node shift

Cells located at the wall of right atrium, near entrance of superior vena cava form the sinoatrial (SA) node which acts as the heart's natural pacemaker. The native rate is constantly modified by activity of sympathetic and parasympathetic nerve fibers.

The origin of pacemaker activity can be shifted by sympathetic and parasympathetic nerve stimulation or changes in extracellular potassium. Shifts in the origin of pacemaker activity will change the pattern of atrial excitation. For instance, stimulation of right sympathetic nerves can shift it rostrally (rotational) within the node and stimulation of vagal nerve can shift it caudally (toward the posterior end) within the SA node and to non-SA-nodal pacemaker[109-111].

Understanding the effect of the nervous system on the control of heart rate, rhythm, and pacemaker location can answer relevant questions related to heart abnormalities, and it will increase our knowledge about autonomic nervous system.

We observed SA node shift in the endocardial activation time mappings during vagal nerve stimulations shown in the figure 3.3, in agreement with previous observations about pacemaker shifts after nerve stimulation [108-110]. Further experimental studies are required to clarify this point.

(A) Without nerve stimulation	(B) With nerve stimulation
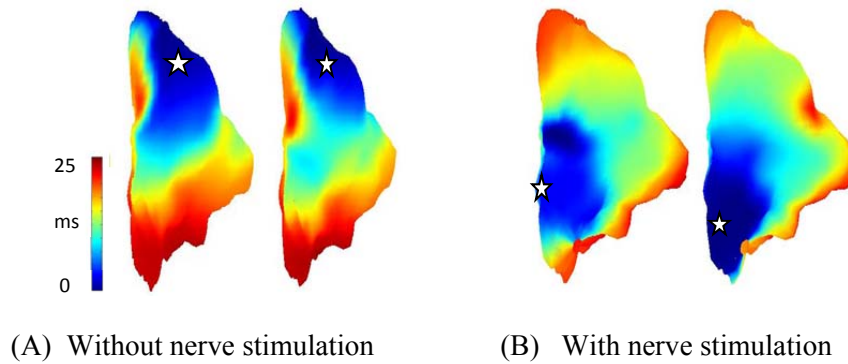
Figure 3.3- (A) The electrical activity starts form the superior portion of right atrium or SVC. (B) It is longer lasting in the peripheral and inferior reigns of the SVC than SA node center. The earliest endocardial activation time is shown by asterisks.

3.3 ATa maps during neurogenically induced AF

To further investigate heart arrhythmias, mapping ATa values during sinus rhythm and neurogenically induced atrial fibrillation would be beneficial. As already mentioned, the ATa provides a quantitative measure to assess atrial repolarization in experimental recordings. Therefore, comparing ATa maps for two heart conditions, sinus rhythm and neurogenically induced atrial fibrillation, might give us a better view on the repolarization gradient changes during heart arrhythmias. In the figure 3.4, the maximum of ATa or repolarization gradient were found in the superior portion of the SVC toward IVC for sinus rhythm. In contrast, ATa maps during nerve stimulation had their maximal value at lower part of right atrium near the right atrium ganglionated plexus.

This preliminary result confirms previous findings that vagal stimulation increases the number of electrode displaying positive ATa[19].

(A) Without nerve stimulation   (B) With nerve stimulation
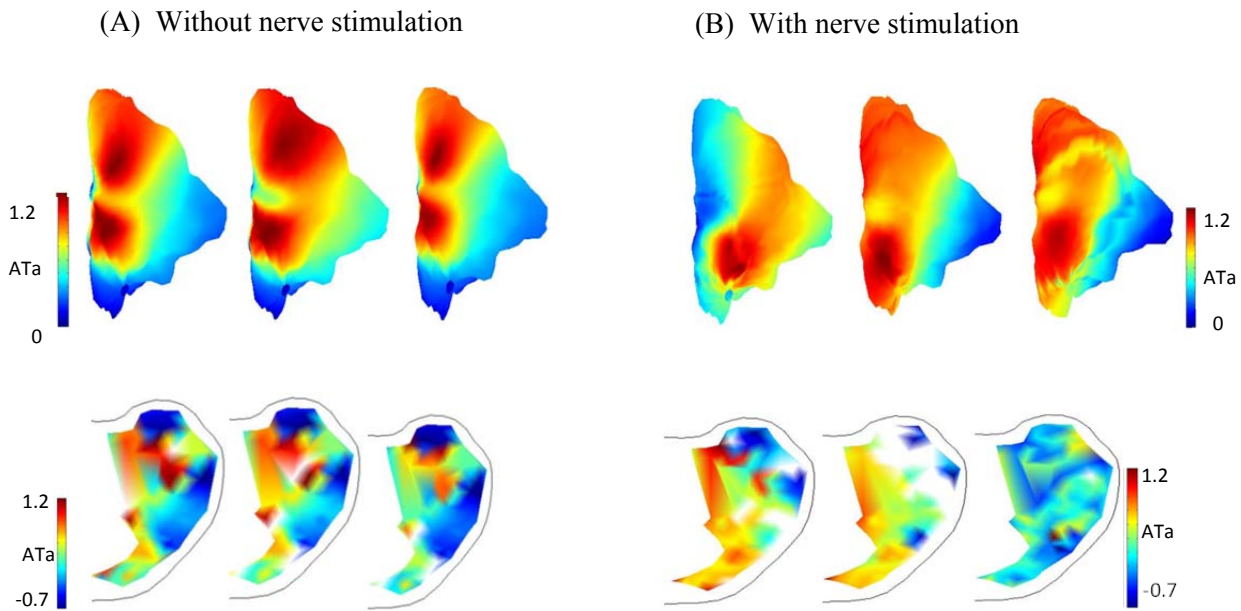
Figure 3.4- The repolarization gradient heterogeneity of the atria during sinus rhythm (A) and neurogenically induced atrial fibrillation (B).

This project was not designed to study ATa and activation time patterns during episodes of neurogenically induced atrial fibrillation. We only focused on validation of non-contact mapping using epicardial mapping by means of activation time and ATa. Therefore, further research is required to investigate repolarization gradient heterogeneity pattern in the atria before and during cardiac arrhythmias.

3.4 Summary of advantages and disadvantages of mapping systems

	Contact epicardial mapping	Noncontact endocardial mapping
Electrode #	• 103 electrodes • 192 electrodes for right and left atria	• 2048 virtual electrodes computed from a 64-channel balloon catheter
Sampling frequency	• 1 kHz	• 1.2 kHz
Inaccessible regions	• Fat pads like right atrium ganglionic plexi • septum	• The measurements are not accurate enough in the appendage
Accessible regions	• Access to right and left atria simultaneously • Inter atria bundle • Bachmann bundle	• Access to one atria at a time • Septum
Activation time maps	• Detection of the activation can be hard due to wide variety of epicardial waveform, notably, in the appendage region	• Noncontact mapping often produced fractionated endocardial waveforms (double potentials) that reduced the accuracy of detected activation times.
ATa maps	• We saw negative and positive ATa values in our recording.	• We saw only positive ATa values in our recording.
Device limitation	• Tissue of the cardiac chamber has to be flattened to suture the epicardial plaques.	• Noncontact mapping has been designed for human; however, it can be applied in the animals if the cardiac chamber is large enough for insertion of balloon catheter. • Inverse problem has to be solved to derived the signals

Table 3.1- Summary of characteristic of contact epicardial mapping and non-contact endocardial mapping.

4 References

1.   Houben RP, Allessie MA. Processing of intracardiac electrograms in atrial fibrillation. Diagnosis of electropathological substrate of AF. IEEE Eng Med Biol Mag 2006;25:40-51.

2.   Murphy DA, Armour JA. Human cardiac nerve stimulation. The Annals of thoracic surgery 1992;54:502-6.

3.   Heart Health Center, Chambers of the Heart. 2012. at http://www.webmd.com/heart/chambers-of-the-heart.)

4.   Widmaier R, Raff H, Strang K. Vander's human physiology: the mechanisms of body function with aris. 2007.

5.   at http://library.thinkquest.org/05aug/01883/functionofheart.htm.)

6.   Heart Anatomy. NewYork-Presbyterian. 2012, at http://nyp.org/health/cardiac-anatomy.html.)

7.   Clinical Anesthesiology, 4th Edition. McGraw-Hill Companies, Inc., 2006. at http://bentollenaar.com/_MM_Book/Ch.19.htm.)

8.   Jacquemet V, Kappenberger L, Henriquez CS. Modeling atrial arrhythmias: Impact on clinical diagnosis and therapies. IEEE Rev Biomed Eng 2008;1:94-114.

9.   Lewis T, Meakins J, White PD. The Excitatory Process in the Dog's Heart. Part I. The Auricles. Philosophical Transactions of the Royal Society of London Series B, Containing Papers of a Biological Character 1914;205:375-420.

10.   Armour JA, Hageman GR, Randall WC. Arrhythmias induced by local cardiac nerve stimulation. Am J Physiol 1972;223:1068-75.

11.   Armour JA, Randall WC, Sinha S. Localized myocardial responses to stimulation of small cardiac branches of the vagus. Am J Physiol 1975;228:141-8.

12.   Hageman GR, Goldberg JM, Armour JA, Randall WC. Cardiac dysrhythmias induced by autonomic nerve stimulation. The American journal of cardiology 1973;32:823-30.

13.   Wilber DJ, Morton JB. Vagal Stimulation and Atrial Fibrillation: Experimental Models and Clinical Uncertainties. Journal of cardiovascular electrophysiology 2002;13:1280-2.

14.   Philip J Podrid M. Reentry and the development of cardiac arrhythmias. 1998.

15.   Medifocus, MediFocus Guide Atrial Fibrillation (Medifocus Guide Series, vol. CR004). Silver Springs, MD: Medifocus Inc, 2005.

16.   Natale A, Jalife J, SpringerLink (Service en ligne). Atrial fibrillation from bench to bedside. Totowa, N.J.: Humana Press; 2008.

17.   Moe GK, Abildskov JA. Atrial fibrillation as a self-sustaining arrhythmia independent of focal discharge. American heart journal 1959;58:59-70.

18.　　Allessie MA, Lammers WJEP, Bonke FIM, Hollen J. Experimental evaluation of Moe?s multiple wavelet hypothesis of atrial fibrillation. In: Zipes DP, Jalife J, editors. Cardiac Arrhythmias; 1985: Grune & Stratton. p. 265-76.

19.　　Vigmond EJ, Tsoi V, Yin Y, Page P, Vinet A. Estimating atrial action potential duration from electrograms. IEEE Trans Biomed Eng 2009;56:1546-55.

20.　　Mandapati R, Skanes A, Chen J, Berenfeld O, Jalife J. Stable microreentrant sources as a mechanism of atrial fibrillation in the isolated sheep heart. Circulation 2000;101:194-9.

21.　　Papageorgiou P, Monahan K, Boyle NG, et al. Site-Dependent Intra-Atrial Conduction Delay: Relationship to Initiation of Atrial Fibrillation. Circulation 1996;94:384-9.

22.　　Natale A, Jalife J. Atrial fibrillation: from bench to bedside: Humana Press; 2008.

23.　　Prat-Gonzalez S, Sanz J, Garcia MJ. Cardiac CT: indications and limitations. Journal of nuclear medicine technology 2008;36:18-24.

24.　　Codreanu A, Odille F, Aliot E, et al. Electroanatomic Characterization of Post-Infarct ScarsComparison With 3-Dimensional Myocardial Scar Reconstruction Based on Magnetic Resonance Imaging. Journal of the American College of Cardiology 2008;52:839-42.

25.　　Earley MJ, Showkathali R, Alzetani M, et al. Radiofrequency ablation of arrhythmias guided by non-fluoroscopic catheter location: a prospective randomized trial. European Heart Journal 2006;27:1223-9.

26.　　Kirchhof P, Loh P, Eckardt L, et al. A novel nonfluoroscopic catheter visualization system (LocaLisa) to reduce radiation exposure during catheter ablation of supraventricular tachycardias. Am J Cardiol 2002;90:340-3.

27.　　Kopelman HA, Prater SP, Tondato F, Chronos NA, Peters NS. Slow pathway catheter ablation of atrioventricular nodal re-entrant tachycardia guided by electroanatomical mapping: a randomized comparison to the conventional approach. Europace 2003;5:171-4.

28.　　Sporton SC, Earley MJ, Nathan AW, Schilling RJ. Electroanatomic versus fluoroscopic mapping for catheter ablation procedures: a prospective randomized study. J Cardiovasc Electrophysiol 2004;15:310-5.

29.　　Kottkamp H, Hugl B, Krauss B, et al. Electromagnetic versus fluoroscopic mapping of the inferior isthmus for ablation of typical atrial flutter: A prospective randomized study. Circulation 2000;102:2082-6.

30.　　Schneider MA, Ndrepepa G, Dobran I, et al. LocaLisa catheter navigation reduces fluoroscopy time and dosage in ablation of atrial flutter: a prospective randomized study. J Cardiovasc Electrophysiol 2003;14:587-90.

31.   Ventura R, Rostock T, Klemm HU, et al. Catheter ablation of common-type atrial flutter guided by three-dimensional right atrial geometry reconstruction and catheter tracking using cutaneous patches: a randomized prospective study. J Cardiovasc Electrophysiol 2004;15:1157-61.

32.   Willems S, Weiss C, Ventura R, et al. Catheter ablation of atrial flutter guided by electroanatomic mapping (CARTO): a randomized comparison to the conventional approach. J Cardiovasc Electrophysiol 2000;11:1223-30.

33.   Estner HL, Deisenhofer I, Luik A, et al. Electrical isolation of pulmonary veins in patients with atrial fibrillation: reduction of fluoroscopy exposure and procedure duration by the use of a non-fluoroscopic navigation system (NavX). Europace 2006;8:583-7.

34.   Derakhchan K, Li D, Courtemanche M, et al. Method for simultaneous epicardial and endocardial mapping of in vivo canine heart: application to atrial conduction properties and arrhythmia mechanisms. Journal of cardiovascular electrophysiology 2001;12:548-55.

35.   Catanchin A, Liew R, Behr ER, Ward DE. Cardiac arrhythmia management using a noncontact mapping multielectrode array. Clinical cardiology 2010;33:E19-E24.

36.   Hindricks G, Kottkamp H. Simultaneous noncontact mapping of left atrium in patients with paroxysmal atrial fibrillation. Circulation 2001;104:297-303.

37.   Schilling RJ, Peters NS, Goldberger J, Kadish AH, Davies DW. Characterization of the anatomy and conduction velocities of the human right atrial flutter circuit determined by noncontact mapping. Journal of the American College of Cardiology 2001;38:385-93.

38.   Earley MJ, Abrams DJR, Sporton SC, Schilling RJ. Validation of the noncontact mapping system in the left atrium during permanent atrial fibrillation and sinus rhythm. Journal of the American College of Cardiology 2006;48:485-91.

39.   Schilling RJ, Kadish AH, Peters NS, Goldberger J, Davies DW. Endocardial mapping of atrial fibrillation in the human right atrium using a non-contact catheter. Eur Heart J 2000;21:550-64.

40.   DIXIT S, LAVI N, ROBINSON M, et al. Noncontact electroanatomic mapping to characterize typical atrial flutter: Participation of right atrial posterior wall in the reentrant circuit. Journal of cardiovascular electrophysiology 2011;22:422-30.

41.   Schilling RJ, Peters NS, Davies DW. Simultaneous endocardial mapping in the human left ventricle using a noncontact catheter: comparison of contact and reconstructed electrograms during sinus rhythm. Circulation 1998;98:887-98.

42.   Tai C-T, Liu T-Y, Lee P-C, Lin Y-J, Chang M-S, Chen S-A. Non-contact mapping to guide radiofrequency ablation of atypical right atrial flutter. Journal of the American College of Cardiology 2004;44:1080-6.

43.   Schmitt H, Weber S, Schwab JO, et al. Diagnosis and ablation of focal right atrial tachycardia using a new high-resolution, non-contact mapping system. American Journal of Cardiology 2001;87:1017-20.

44.   Friedman PA, Asirvatham SJ, Grice S, et al. Noncontact mapping to guide ablation of right ventricular outflow tract tachycardia. Journal of the American College of Cardiology 2002;39:1808-12.

45.   Ribbing M, Wasmer K, Mönnig G, et al. Endocardial mapping of right ventricular outflow tract tachycardia using noncontact activation mapping. Journal of cardiovascular electrophysiology 2003;14:602-8.

46.   Cohen TJ, Juang G, Daggubati R. Utility of non-contact three-dimensional mapping of the left atrium for ablation of left atrial tachycardia. The Journal of invasive cardiology 2004;16:100-1.

47.   Earley MJ, Abrams DJ, Sporton SC, Schilling RJ. Validation of the noncontact mapping system in the left atrium during permanent atrial fibrillation and sinus rhythm. Journal of the American College of Cardiology 2006;48:485-91.

48.   Yao Y, Zheng L, Zhang S, et al. Stepwise linear approach to catheter ablation of atrial fibrillation. Heart Rhythm 2007;4:1497-504.

49.   Chen J, Hoff PI, Erga KS, Rossvoll O, Ohm OJ. Three-dimensional noncontact mapping defines two zones of slow conduction in the circuit of typical atrial flutter. Pacing Clin Electrophysiol 2003;26:318-22.

50.   Dixit S, Lavi N, Robinson M, et al. Noncontact electroanatomic mapping to characterize typical atrial flutter: participation of right atrial posterior wall in the reentrant circuit. J Cardiovasc Electrophysiol 2011;22:422-30.

51.   Schilling RJ, Peters NS, Goldberger J, Kadish AH, Davies DW. Characterization of the anatomy and conduction velocities of the human right atrial flutter circuit determined by noncontact mapping. J Am Coll Cardiol 2001;38:385-93.

52.   Krum D, Goel A, Hauck J, et al. Catheter location, tracking, cardiac chamber geometry creation, and ablation using cutaneous patches. Journal of interventional cardiac electrophysiology 2005;12:17-22.

53.   Abrams DJ, Earley MJ, Sporton SC, et al. Comparison of noncontact and electroanatomic mapping to identify scar and arrhythmia late after the Fontan procedure. Circulation 2007;115:1738-46. Epub 2007 Mar 19.

54.   Thiagalingam A, Wallace EM, Boyd AC, et al. Noncontact Mapping of the Left Ventricle. Pacing and clinical electrophysiology 2004;27:570-8.

55.   Haissaguerre M, Jais P, Shah DC, et al. Spontaneous initiation of atrial fibrillation by ectopic beats originating in the pulmonary veins. N Engl J Med 1998;339:659-66.

56.   Hilgemann D, Noble D. Excitation-contraction coupling and extracellular calcium transients in rabbit atrium: reconstruction of basic cellular mechanisms. Proceedings of the Royal society of London Series B Biological sciences 1987;230:163-205.

57.   Lindblad D, Murphey C, Clark J, Giles W. A model of the action potential and underlying membrane currents in a rabbit atrial cell. American Journal of Physiology-Heart and Circulatory Physiology 1996;271:H1666-H96.

58.   Nygren A, Fiset C, Firek L, et al. Mathematical model of an adult human atrial cell the role of k+ currents in repolarization. Circulation Research 1998;82:63-81.

59.   Courtemanche M, Ramirez RJ, Nattel S. Ionic mechanisms underlying human atrial action potential properties: insights from a mathematical model. Am J Physiol 1998;275:301.

60.   Virag N, Jacquemet V, Henriquez CS, et al. Study of atrial arrhythmias in a computer model based on magnetic resonance images of human atria. Chaos 2002;12:754-63.

61.   van Dam PM, van Oosterom A. Atrial excitation assuming uniform propagation. J Cardiovasc Electrophysiol 2003;14:166.

62.   Ridler M, McQueen DM, Peskin CS, Vigmond E. Action potential duration gradient protects the right atrium from fibrillating. Conf Proc IEEE Eng Med Biol Soc 2006;1:3978-81.

63.   Spitzer VM, Whitlock DG. The Visible Human Dataset: the anatomical platform for human simulation. Anat Rec 1998;253:49-57.

64.   Freudenberg J, Schiemann T, Tiede U, Höhne K. Simulation of cardiac excitation patterns in a three-dimensional anatomical heart atlas. Computers in Biology and Medicine 2000;30:191-205.

65.   Zemlin CW, Herzel H, Ho SY, Panfilov A. A realistic and efficient model of excitation propagation in the human atria. In: Virag N, Blanc O, Kappenberger L, editors. Computer Simulation and Experimental Assessment of Cardiac Electrophysiology; 2001: Armonk, NY: Futura Publishing. p. 29-34.

66.   Seemann G, Hoper C, Sachse FB, Dossel O, Holden AV, Zhang H. Heterogeneous three-dimensional anatomical and electrophysiological model of human atria. Philos Transact A Math Phys Eng Sci 2006;364:1465-81.

67.   Seemann G, Höper C, Sachse FB, Dössel O, Holden AV, Zhang H. Heterogeneous three-dimensional anatomical and electrophysiological model of human atria. Philosophical Transactions of the Royal Society A: Mathematical, Physical and Engineering Sciences 2006;364:1465-81.

68.   Courtemanche M, Ramirez RJ, Nattel S. Ionic targets for drug therapy and atrial fibrillation-induced electrical remodeling: insights from a mathematical model. Cardiovasc Res 1999;42:477-89.

69.   Kuo SR, Trayanova NA. Action potential morphology heterogeneity in the atrium and its effect on atrial reentry: a two-dimensional and quasi-three-dimensional study. Philos Transact A Math Phys Eng Sci 2006;364:1349-66.

70.   Cherry EM, Ehrlich JR, Nattel S, Fenton FH. Pulmonary vein reentry—properties and size matter: insights from a computational analysis. Heart Rhythm 2007;4:1553-62.

71.   Vigmond EJ, Tsoi V, Kuo S, et al. The effect of vagally induced dispersion of action potential duration on atrial arrhythmogenesis. Heart Rhythm 2004;1:334-44.

72.   Gulrajani RM. The forward and inverse problems of electrocardiography. Engineering in Medicine and Biology Magazine, IEEE 1998;17:84-101, 22.

73.   computational   electrocardiography.   2013.   at http://matthijs.cluitmans.net/academic/documents/53-thesis.)

74.   Computational   Electrocardiography.   2012,   at http://matthijs.cluitmans.net/academic/documents/53-msc-thesis.)

75.   Salinet Jr JL, Oliveira GN, Vanheusden FJ, Comba JLD, Ng GA, Schlindwein FS. Visualizing Intracardiac Atrial Fibrillation Electrograms Using Spectral Analysis. Computing in Science & Engineering 2013;15:79-87.

76.   Goldberger JJ, Ng J. Practical signal and image processing in clinical cardiology: Springer; 2010.

77.   Ndrepepa G, Caref EB, Yin H, El-SHERIF N, Restivo M. Activation Time Determination by High-Resolution Unipolar and Bipolar Extracellular Electrograms in the Canine Heart. Journal of cardiovascular electrophysiology 1995;6:174-88.

78.   Myerburg RJ, Nilsson K, Zoble RG. Relationship of surface electrogram recordings to activity in the underlying specialized conducting tissue. Circulation 1972;45:420-32.

79.   Haws CW, Lux RL. Correlation between in vivo transmembrane action potential durations and activation-recovery intervals from electrograms. Effects of interventions that alter repolarization time. Circulation 1990;81:281-8.

80.   Schuessler RB, Kawamoto T, Hand DE, et al. Simultaneous epicardial and endocardial activation sequence mapping in the isolated canine right atrium. Circulation 1993;88:250-63.

81.   Armour JA, Richer L-P, Pagé P, et al. Origin and pharmacological response of atrial tachyarrhythmias induced by activation of mediastinal nerves in canines. Autonomic Neuroscience 2005;118:68-78.

82.   Pagé PL, Dandan N, Savard P, Nadeau R, Armour JA, Cardinal R. Regional distribution of atrial electrical changes induced by stimulation of extracardiac and intracardiac neural elements. The Journal of Thoracic and Cardiovascular Surgery 1995;109:377-88.

83.   Cardinal R, Armour JA, Bouchard C, et al. Atrial Tachyarrhythmias and Repolarization Changes Induced by Discrete Activation of Dorsal Mediastinal Cardiac Nerves in Canines. Circ Arrhythm Electrophysiol 2010 (in press).

84. Schotten U, Verheule S, Kirchhof P, Goette A. Pathophysiological mechanisms of atrial fibrillation: a translational appraisal. Physiol Rev 2011;91:265-325.

85. Efimov IR, Fedorov VV. Chessboard of atrial fibrillation: reentry or focus? Single or multiple source(s)? Neurogenic or myogenic? Am J Physiol Heart Circ Physiol 2005;289:H977-9.

86. Armour JA, Ardell JL. Basic and Clinical Neurocardiology. New York: Oxford University Press; 2004.

87. Jacquemet V. An Eikonal Approach for the Initiation of Reentrant Cardiac Propagation in Reaction-Diffusion Models. IEEE Trans Biomed Eng 2010;57:2090-8.

88. Cardinal R, Armour JA, Bouchard C, et al. Atrial tachyarrhythmias and repolarization changes induced by discrete activation of dorsal mediastinal cardiac nerves in canines. Circ Arrhythm Electrophysiol 2010;3:511-20.

89. Page P, Andrew Armour J, Yin Y, Vermeulen M, Nadeau R, Cardinal R. Differential effects of cervical vagosympathetic and mediastinal nerve activation on atrial arrhythmia formation in dogs. Auton Neurosci 2006;128:9-18.

90. Page PL, Dandan N, Savard P, Nadeau R, Armour JA, Cardinal R. Regional distribution of atrial electrical changes induced by stimulation of extracardiac and intracardiac neural elements. J Thorac Cardiovasc Surg 1995;109:377-88.

91. Armour JA, Richer LP, Page P, et al. Origin and pharmacological response of atrial tachyarrhythmias induced by activation of mediastinal nerves in canines. Auton Neurosci 2005;118:68-78.

92. Catanchin A, Liew R, Behr ER, Ward DE. Cardiac arrhythmia management using a noncontact mapping multielectrode array. Clin Cardiol 2010;33:E19-24.

93. Juneja R. Radiofrequency ablation for cardiac tachyarrhythmias: principles and utility of 3D mapping systems. Curr Sci 2009;97:416-24.

94. Earley MJ, Abrams DJ, Sporton SC, Schilling RJ. Validation of the noncontact mapping system in the left atrium during permanent atrial fibrillation and sinus rhythm. J Am Coll Cardiol 2006;48:485-91.

95. Abrams DJ, Earley MJ, Sporton SC, et al. Comparison of noncontact and electroanatomic mapping to identify scar and arrhythmia late after the Fontan procedure. Circulation 2007;115:1738-46.

96. Voth EJ. The inverse problem of electrocardiography: industrial solutions and simulations. Int J Bioelectromagn 2005;7:191-4.

97. Herlin A, Jacquemet V. Eikonal-based initiation of fibrillatory activity in thin-walled cardiac propagation models. Chaos 2011;21:043136.

98.   Krueger M, Schmidt V, Tobón C, et al. Modeling Atrial Fiber Orientation in Patient-Specific Geometries: A Semi-automatic Rule-Based Approach. Functional Imaging and Modeling of the Heart; 2011: Springer. p. 223-32.

99.   Gulrajani RM. Bioelectricity and Biomagnetism. New York: John Wiley & Sons; 1998.

100.   Buzzard GT, Fox JJ, Siso-Nadal F. Sharp interface and voltage conservation in the phase field method: application to cardiac electrophysiology. SIAM J Sci Comput 2008;30:837.

101.   Kneller J, Zou R, Vigmond EJ, Wang Z, Leon LJ, Nattel S. Cholinergic atrial fibrillation in a computer model of a two-dimensional sheet of canine atrial cells with realistic ionic properties. Circ Res 2002;90:73.

102.   Ramirez RJ, Nattel S, Courtemanche M. Mathematical analysis of canine atrial action potentials: rate, regional factors, and electrical remodeling. Am J Physiol Heart Circ Physiol 2000;279:1767.

103.   Jacquemet V, Virag N, Ihara Z, et al. Study of unipolar electrogram morphology in a computer model of atrial fibrillation. J Cardiovasc Electrophysiol 2003;14:172.

104.   Harley D, Greenfield P, Amariglio L, inventors; Non-contact cardiac mapping, including preprocessing patent US 7,505,810 B2. 2009.

105.   de Munck JC. A linear discretization of the volume conductor boundary integral equation using analytically integrated elements. IEEE Trans Biomed Eng 1992;39:986-90.

106.   van Oosterom A. Closed-form analytical expressions for the potential fields generated by triangular monolayers with linearly distributed source strength. Med Biol Eng Comput 2012;50:1-9.

107.   Dube B, Vinet A, Xiong F, Yin Y, LeBlanc AR, Page P. Automatic detection and classification of human epicardial atrial unipolar electrograms. Physiol Meas 2009;30:1303-25.

108.   Botev ZI, Grotowski JF, Kroese DP. Kernel density estimation via diffusion. Ann Statist 2010;38:2916-57.

109.   Goldberg JM. Intra-SA-nodal pacemaker shifts induced by autonomic nerve stimulation in the dog. American Journal of Physiology--Legacy Content 1975;229:1116-23.

110.   Schuessler RB, Boineau JP, Wylds AC, Hill DA, Miller CB, Roeske WR. Effect of canine cardiac nerves on heart rate, rhythm, and pacemaker location. American Journal of Physiology-Heart and Circulatory Physiology 1986;250:H630-H44.

111.   Shibata N, Inada S, Mitsui K, et al. Pacemaker shift in the rabbit sinoatrial node in response to vagal nerve stimulation. Experimental physiology 2001;86:177-84.